Geochimica et Cosmochimica Acta 359 (2023) 1–19

Contents lists available at ScienceDirect

Geochimica et Cosmochimica Acta

journal homepage: www.elsevier.com/locate/gca

Sulfur and chlorine in nakhlite clinopyroxenes: Source region concentrations and magmatic evolution

Don R. Baker [a,*], Sara Callegaro [b,c], Andrea Marzoli [d], Angelo De Min [e], Kalotina Geraki [f], Martin J. Whitehouse [g], Agata M. Krzesinska [b,c], Anna Maria Fioretti [h]

[a] McGill University, Department of Earth and Planetary Sciences, Montréal, Quebec, Canada
[b] Centre for Earth Evolution and Dynamics (CEED), University of Oslo, Sem Sælands vei, 2A N-0371 Oslo, Norway
[c] Centre for Planetary Habitability (PHAB), University of Oslo, Sem Sælands vei 2A, N-0371 Oslo, Norway
[d] University of Padova, Department of Land, Environment, Agriculture and Forestry, Legnaro, Italy
[e] Department of Mathematics and Geoscience, University of Trieste, via Weiss 2, 34128 Trieste, Italy
[f] Diamond Light Source, Harwell Science and Innovation Campus, Didcot OX11 0DE, UK
[g] Swedish Museum of Natural History, Stockholm, Sweden
[h] Instituto di Scienze Polari CNR, Padova, Italy

ARTICLE INFO

Associate editor: Christopher Herd

Keywords:
Mars
Nakhlite
Sulfur
Chlorine
Fluorine
Clinopyroxene
MIL 03346
Nakhla
NWA 998

ABSTRACT

The volatile concentrations of the martian mantle and martian magmas remain important questions due to their role in petrogenesis and planetary habitability. The sulfur and chlorine concentrations, and their spatial distribution, in clinopyroxenes from nakhlites MIL 03346, Nakhla, and NWA 998 were measured to provide insight into these volatiles in the parental melts and source regions of nakhlites, and to constrain the evolution of the nakhlite melts. Sulfur and chlorine in four clinopyroxene crystals from MIL 03346, four from Nakhla, and five from NWA 998 were measured in crystal cores and rims by synchrotron X-ray fluorescence using beamline I18 at the Diamond Light Source. Portions of two crystals from MIL 03346 and one from Nakhla were mapped for S and Cl; a few reconnaissance analyses of Cl and F in MIL 03346 and Nakhla were made by ion microprobe. Clinopyroxene cores in Nakhla and NWA 998 contain ~10 ppm S, ~10 ppm Cl and ~74 ppm F (only Nakhla analyzed), whereas the cores of MIL 03346 contain ~10 ppm S, ~5 ppm Cl and ~53 ppm F.

Using the volatile concentrations in the cores combined with previously determined partition coefficients we calculate that these clinopyroxenes crystallized from evolved basaltic melts containing ~500 ppm S, ~500–1900 ppm Cl, and 160–420 ppm F. These evolved melts can be used to calculate primitive melts in equilibrium with martian peridotite and the concentrations of S, Cl and F in the mantle source region of the nakhlite melts. Depending upon the extent of melting (5–30%) necessary to produce the primary melts associated with nakhlites, our calculations indicate that the nakhlite source region has a S concentration between 20 (5% melting) to 120 ppm (30% melting), Cl between 16 and 97 ppm, and F between 14 and 48 ppm. These concentrations in the nakhlite magma source region are similar to previous estimates for the martian mantle; our calculated source region concentrations of F and Cl agree best with previous estimates if the martian mantle undergoes 10–20% melting to produce primary magmas that evolve to be parental to nakhlites. However, our maximum estimated sulfur concentration of the source (calculated for 30% melting) is near previous minimum estimates for the martian mantle, suggesting the possibility that the nakhlite source region is depleted in sulfur relative to much of Mars' mantle.

Mapping the spatial distribution of volatiles in three clinopyroxene crystals demonstrates that S and Cl concentrations of the evolving melts changed significantly from the core to the rim, particularly those in MIL 03346. Increasing S and Cl concentrations between the core and rim of MIL 03346 crystals are attributed to incorporation of additional volatiles through assimilation, but the Nakhla crystal shows no such evidence. However, concentrations of Cl and S at some outer crystal rims of one MIL 03346 crystal decrease, most probably due to volatile degassing during the final stages of clinopyroxene growth.

* Corresponding author.
E-mail address: don.baker@mcgill.ca (D.R. Baker).

https://doi.org/10.1016/j.gca.2023.08.007
Received 13 June 2022; Accepted 1 August 2023
Available online 9 August 2023

1. Introduction

Igneous processes are the fundamental mechanism for the transport of volatiles from the interior to the surface and atmosphere of terrestrial planets (e.g., Ding et al., 2015; Filiberto et al., 2016, 2019). Analysis of volatiles in igneous rocks from other planets provides insight into their storage and transport, and into the potential geodynamic scenarios occurring in the planet (e.g., Albarède, 2009). This research investigates the magmatic behavior of S and Cl. Because volatiles play a fundamental role in life, improved understanding of their behavior in planetary bodies provides information useful for the determination of habitability. And although water is the primary volatile required for life as we know it, sulfur and chlorine also play important biochemical roles: Sulfur is involved in biochemical processes in bacteria, plants, and animals (e.g., Dahl and Friedrich, 2008; Jørgensen, 2021), and chlorine is a charge balancing anion and acts as an energy supply in some microorganisms (Barnum and Coates, 2022).

The high concentrations of sulfur and chlorine in martian surficial deposits (Boynton et al., 2007; Morrison et al., 2018; Filiberto et al., 2019; Certini et al., 2020; Rampe et al., 2020) may indicate that the quantities of these volatiles are significant in igneous rocks, and that martian igneous source regions are more enriched in these volatiles than terrestrial ones. Martian melts have been shown to have the ability to transport high concentrations of sulfur (Righter et al., 2009; Ding et al., 2015), and weight percent levels of chlorine in martian melts have been inferred from high-temperature experiments and meteorite analyses (Filiberto and Treiman, 2009a,b).

Traditionally, volatile concentrations in Mars' interior have been estimated by bulk analyses of martian meteorites with igneous textures (shergottites, nakhlites, and chassignites) or calculated using mixtures of different types of chondrites presumed to have formed the planet (e.g., Dreibus and Wänke, 1987; Wänke and Dreibus, 1988, Lodders and Fegley, 1997; Sanloup et al., 1999; Ding et al., 2015; Yoshizaki and McDonough, 2020). More recently, concentrations in volatile-bearing minerals such as apatite, scapolite, and amphibole have been used for the same purpose (e.g., McCubbin et al., 2013, 2016; Filiberto et al., 2014, 2016).

However, the range of concentrations of volatile elements in meteorites can be vast; consider, for example, sulfur. The bulk-rock sulfur concentrations in martian meteorites vary from 34 ppm to 2865 ppm (Ding et al., 2015). Some of the variation is no doubt due to heterogeneities in the samples analyzed, different source regions for the igneous meteorites, and the fraction of cumulate crystals present. However, even co-genetic nakhlites (Treiman, 2005; McCubbin et al., 2013; Udry and Day, 2018) with estimated cumulate fractions varying only between 0.7 and 0.85 display highly variable sulfur concentrations, from 34 ppm to 1287 ppm (Ding et al., 2015). Furthermore, isotopic analyses of multiple nakhlites demonstrate that some sulfur in the rocks has a mass-independent isotopic signature, suggesting that atmospheric sulfur was incorporated through assimilation of near-surface rocks (Farquhar et al., 2000; Franz et al., 2014, 2019; Mari et al., 2019) and therefore may not reflect source region concentrations. Nakhlites also display evidence of hydrous, subsolidus alteration (Gillet et al., 2002; Treiman, 2005; Udry and Day, 2018), which in most cases occurred at low temperatures, but in some cases are inferred to have occurred at temperatures up to 900 °C (Sautter et al., 2006; Noguchi et al., 2009; Filiberto et al., 2014). Both high- and low-temperature processes may have caused sulfur enrichment in the bulk rocks. Hence, the complex history of nakhlites hinders a straightforward assessment of the sulfur in their parental melts and source regions from bulk-rock analyses.

The complications involved in inverse modeling of the volatile concentrations in the martian interior from meteorites result in estimates of martian mantle concentrations of sulfur ranging from 86 to 2000 ppm (Steenstra and van Westrenen, 2018; Gaillard et al., 2013, respectively), of chlorine from 2 to 160 ppm (Filiberto et al., 2019; Lodders and Fegley, 1997, respectively), and of fluorine from 1 to 41 ppm (Filiberto et al., 2019; Lodders and Fegley, 1997, respectively). Given this wide range of concentrations we asked the question: "What are the best estimates of the concentrations of S and Cl in the nakhlite source region, and how do these volatiles evolve in the magmatic system that produced nakhlite meteorites?" Answers to these questions shed light on processes in martian magmatic systems and on the evolution of the whole planet (e.g., Steenstra and van Westrenen, 2018) and have the potential to be used in future studies of Mars' habitability.

In this study we measured the concentrations of volatiles in nakhlite clinopyroxene crystals at micrometer-scale spatial resolution (microbeam analysis) and combined those measurements with mineral/melt partition coefficients to constrain the volatile concentrations in parental melts and in martian magmatic source regions (cf., McCubbin et al., 2013; Peslier et al., 2019). In-situ analysis can avoid the bias in whole-rock analyses caused by cumulate crystals and by secondary alteration. Microbeam analysis also can investigate the evolution of volatile concentrations in evolving melts through analyses of different parts of the same crystal (e.g., from the cores to the rims). This may lead to an improved understanding of the assimilation process responsible for the sulfur (Farquhar et al., 2000; Franz et al., 2014, 2019; Mari et al., 2019) and chlorine (Shearer et al., 2018) isotopic signatures seen in martian meteorites.

We analyzed the cores of 13 clinopyroxenes from three different nakhlites (Nakhla, NWA 998, and MIL 03346) using synchrotron X-ray microfluorescence (SXRF) to better understand the concentrations of S and Cl in the parental melts of nakhlite meteorites and their source regions. We also performed a few preliminary ion microprobe analyses of F and Cl with the same goal. These measurements combined with crystal/melt partition coefficients and partial melting models provide an independent estimate of the concentrations of these volatiles in the nakhlite parental melts and their source region. Additionally, clinopyroxene has the potential to record the evolution of S and Cl in residual melts during the progress of crystallization (unlike the very rare melt inclusions in silicate minerals or volatile concentrations in phosphates, which record the S and Cl concentrations at their moment of entrapment or crystallization). The S and Cl evolution was calculated from point analyses of crystal cores and rims, and compositional mapping of S and Cl in three clinopyroxenes. This was done to investigate the effect of the previously proposed assimilation of a S-rich, near-surface reservoir (Farquhar et al., 2000; Franz et al., 2014, 2019; Mari et al., 2019) and Cl-rich fluid (Sautter et al., 2006; McCubbin et al., 2013) by nakhlite magmas and for evidence of degassing during the final stages of crystallization (Sautter et al., 2006; Giesting and Filiberto, 2016; Peslier et al., 2019).

2. Samples and techniques

2.1. Samples

Three nakhlite meteorites were investigated in this study: Nakhla, NWA 998, and MIL 03346. Nakhlites are olivine-bearing, clinopyroxene cumulates believed to be from a single magmatic system (e.g., Treiman, 2005; Day et al., 2006; Goodrich et al., 2013; Peslier et al., 2019; Udry and Day, 2018) and to have experienced minor shock metamorphism, with bulk pressures in the range of 5–16 GPa (e.g., Fritz et al., 2005a,b; Treiman and Irving, 2008; Day et al.; 2006; Jambon et al., 2016; Daly et al., 2019). Indeed, Daly et al. (2019) explicitly state that the nakhlites' microstructures "are characteristic of mild shock metamorphism".

Investigating three different samples from what appears to be a single magmatic system (see Udry and Day, 2018, for a recent summary) has the advantage of providing multiple assessments of the volatile (S, Cl, and F) concentrations of the source region, considered to be the martian mantle (Treiman, 2005, Day et al., 2006, 2018; Goodrich et al., 2013; McCubbin et al., 2013; Peslier et al., 2019; Udry and Day, 2018), although we note that the evolution of MIL 03346 is known to be different in some respects from that of Nakhla and NWA 998 (Day et al.,

2006; Sautter et al., 2006; McCubbin et al., 2009; Giesting and Filiberto, 2016; Udry and Day, 2018). The calculated volatile concentrations in nakhlite parental magmas and the source region appear to be only representative of one single locality (e.g., Udry and Day, 2018) and one region of the martian mantle at one specific moment of the geological history of the planet. Nevertheless, relatively poorly-shocked meteorites provide the best samples for the evaluation of unaltered, igneous volatile concentrations.

Recent studies of nakhlite microstructures (Daly et al., 2019; Martell et al., 2022) show spatial correlations between localized shock features and alteration products. This could imply that igneous volatiles may have been redistributed by shock and aqueous alteration. To address this, the least shocked crystals of augite were chosen for analysis. The analyzed crystals are located in small, apparently unaltered mesostasis patches, where no significant shock wave reverberations would be expected. The grains appear unfractured and no mosaic or undulose extinction (attributable to shock) was observed. Additionally, optical microscopy and scanning electron imaging of the analyzed crystals displayed no evidence of veins associated with hydrothermal alteration (e.g., Treiman, 2005; Stopar et al., 2013; Udry and Day, 2018). However, the clinopyroxenes contain cracks that, as discussed below, are associated with volatile-enriched regions in some crystals that maybe be due to minor post-magmatic alteration. (We either avoided making analyses near cracks, or when that was unavoidable discarded the analyses close to the cracks, as discussed below and in Appendix A. Supplementary Material.)

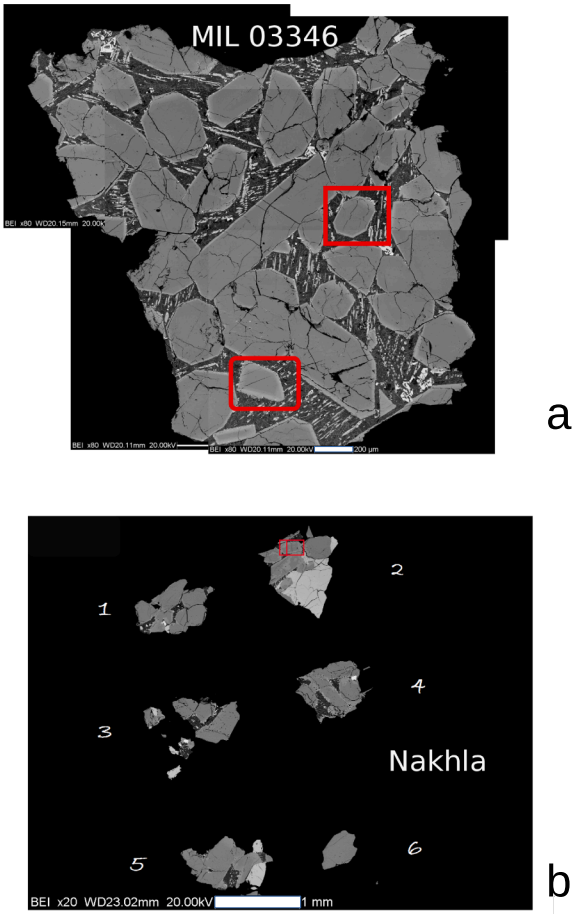

Fig. 1. Backscattered electron images of nakhlite thin sections analyzed in this study. (a) Mosaic of backscattered images of MIL 03346. (b) Backscattered image of Nakhla. (c) Backscattered image of NWA 998. The two crystals mapped in MIL 03346 and the one in Nakhla are identified by the red squares or rectangle in panels a and b. Also shown in red in panel b is one of the analytical traverses made on the Nakhla crystal. Almost all crystals in each panel are clinopyroxenes (medium gray). We have not analyzed all the lighter gray crystals in the mesostasis, but the ones that we have investigated by EDS are iron–titanium oxides.

The nakhlite samples analyzed in this study, MIL 03346, 13; Nakhla (BM 1913, 25), and NWA 988, were previously studied by Carraro et al. (2010), Domeneghetti et al. (2013), Alvaro et al. (2015), and Murri et al. (2016, 2019). They were provided to us as thin section (MIL 03346) and polished mounts of disaggregated grains (Nakhla and NWA 988) (Fig. 1).

2.2. Scanning electron microscope (SEM) imaging and electron microprobe (EMP) analysis

Backscattered images of the prepared sections (Fig. 1) were obtained on a Camscan XM2500 scanning electron microscope (SEM) equipped with a EDAX-Phoenix system and with a Tescan Solaris Field-Emission SEM equipped with the Ultim max 65 Oxford Instrument silicon drift EDS detector; both instruments were at the Department of Geosciences, University of Padova. Major element compositions of clinopyroxenes (Appendix A. Supplementary Material) were obtained by electron microprobe analysis with a CAMECA SX50 at the Istituto di Geoscienze e Georisorse CNR, Padova, Italy, operating at an accelerating voltage of 15 kV and a beam current of 5–20 nA, with 10–40 sec acquisition times. Amelia albite was used as the standard for Na and Al, periclase for Mg, diopside for Si and Ca, orthoclase for K, eskolaite for Cr, pyrophanite for Mn and Ti, and hematite for Fe. Routine ZAF (Z–atomic number; A–absorption; F–fluorescence) on-line data reduction and matrix correction procedures were applied. The size of the analytical spot was ca. 1 μm. Analytical uncertainties are estimated to be lower than 1 and 5% relative for major and minor elements, respectively.

2.3. Synchrotron X-ray fluorescence (SXRF) analysis

Because the electron microprobe is unsuitable for elemental analyses at low, 10′s of ppm, concentration levels, point analyses and mapping of sulfur and chlorine in the clinopyroxene crystals were performed by synchrotron X-ray fluorescence (SXRF). This non-destructive technique allows analysis of trace elements at concentrations down to the parts per million level at micrometer-scale spatial resolution. SXRF analyses were done on Beamline I18 at the Diamond Synchrotron Light Source (Oxfordshire, England) following the procedures of Callegaro et al. (2020). Synchrotron X-ray fluorescence was performed in a helium atmosphere with a 3 keV beam focused to 6 μm × 6 μm by a pair of Kirkpatrick-Baez mirrors; fluorescence spectra were measured for 200 s live time by a Vortex silicon drift detector. Sulfur and chlorine concentrations were determined from the spectra using the software package PyMca (Solé et al., 2007) and using the silicon concentration of the minerals as the internal reference for quantification.

The detection limit of sulfur and chlorine was calculated to be ~1 ppm (p. 446, Goldstein et al., 2003; Rousseau, 2001). Based upon a relative uncertainty of 10% in our electron microprobe analyses as well as 10% uncertainty seen in our peak fitting areas, we calculate through error propagation (Rousseau, 2001) an analytical uncertainty of 14% relative (1-sigma) for samples with 6 ppm and greater. At 2 ppm sulfur, the uncertainty in the peak fitting areas reaches 37% and the analytical uncertainty becomes 38% relative (1-sigma). This technique was tested using an in-house basaltic glass secondary standard previously analyzed by electron microprobe. The mean sulfur concentration measured in multiple locations by electron microprobe was 103 ± 35 (1-sigma) ppm and by SXRF was 100 ± 11 (1-sigma) ppm. The mean chlorine concentration of the analytical locations in this glass was 537 ± 42 (1-sigma) ppm and 607 ± 32 (1-sigma) ppm when analyzed by the electron microprobe and SXRF, respectively. Although the difference in Cl analyses by the two different techniques is significant, it is less than our SXRF analytical uncertainty of 14%, and thus the two different types of analyses are statistically indistinguishable.

The SXRF analytical technique for sulfur was also tested at low concentration levels by analysis of two clinopyroxene crystals previously analyzed by bulk-rock techniques to check our SXRF results, *gem*-quality DeKalb diopside (USNM #R18685) and slightly zoned F-14 clinopyroxene (Frosty Peak, AK, USA, collected by D.R.B.). Bulk analyses of these crystals for sulfur were made at the Saskatchewan Research Council Geoanalytical Laboratories using an Eltra HELIOS carbon and sulfur analyzer. Three aliquots of DeKalb diopside had a mean sulfur concentration of 32 ± 15 ppm (1-standard deviation) and one aliquot of F-14 clinopyroxene had 32 ppm sulfur. Eight SXRF analyses of DeKalb diopside crystals contained 32 ± 18 ppm S and six analyses of F-14 clinopyroxene had 22 ± 9 ppm sulfur. The agreement of bulk sulfur analyses and the average of the SXRF analyses is within 1-σ uncertainty for DeKalb and just outside the 1-σ uncertainty for F-14, although both crystals display heterogeneity in sulfur concentrations.

We lacked suitable clinopyroxene crystals to assess the SXRF analyses of chlorine at low concentration levels. However, as discussed below in Section 3.1.1, the concentrations of chlorine in clinopyroxene crystals MIL 03346 D1 and D4 far from cracks analyzed by both SXRF and by ion microprobe are similar, with the exception of one analysis in the core of D4 (Table 1). Concentrations of chlorine measured by SXRF in the core of Nakhla clinopyroxene 2-1 are mostly between 10 and 14 ppm, whereas the 3 ion probe analyses are between 3 and 4 ppm Cl (Table 1). We attribute the differences between SXRF and ion probe analyses of chlorine to micrometer-scale compositional heterogeneities in the crystals, but cannot rule out the possibility of a systematic difference between the ion probe and SXRF analyses for Cl. In this work we rely upon the SXRF analyses for Cl, but recognize the need for future research comparing and intercalibrating the results of SXRF and ion microprobe, which is beyond the scope of this contribution.

2.3.1. SXRF mapping

Map analyses were made with the same 6 μm × 6 μm beam size as used for the point analyses and moving the sample stage in the x- and y-directions using 20 μm steps. The live time for each location was 50 s. PyMca produces a quantified map of S and Cl concentrations whose pixels are the size of the analytical steps, 20 μm × 20 μm. This map was then scaled to, and superimposed upon, the backscattered images of the crystals. Although this produces a map with adjoining pixels, the analyses only represent the center 6 μm × 6 μm region of each pixel in the map. These maps were used to determine the S and Cl concentrations along the same profiles as used for major element (electron microprobe) traverses. In most cases, the maps were at an angle to the electron microprobe traverses and the concentrations along these traverses were calculated using the "improfile" command with a bilinear interpolation in Matlab®.

2.4. Secondary Ion Mass Spectrometry (SIMS or ion microprobe)

A few reconnaissance analyses of fluorine and chlorine in the clinopyroxenes were performed by Secondary Ion Mass Spectrometry using a large geometry CAMECA IMS 1280 instrument at the Nordsim facility, Swedish Museum of Natural History, Stockholm (Sweden). The analytical protocol was described in more detail by Baker et al. (2022) and used a $^{133}Cs^{+}$ primary beam of ~0.5 nA with an accelerating voltage of −10 kV together with low-energy, normal-incidence electron flooding to counteract charge buildup on the target. Each analysis began by rastering the primary beam over a 20 μm × 20 μm area for 120 s to remove the gold coating and surface contamination. The beam was then reduced to a ~10 μm × 10 μm raster for data acquisition. The secondary ions were accelerated with a −10 kV potential, centered in the field aperture, and optimized using the ^{18}O signal. The mass resolution (M/ΔM) was 2430 and ions were measured by magnet peak switching on a low-noise, ion-counting electron multiplier. Ratios of $^{19}F/^{18}O$ and $^{35}Cl/^{18}O$ were used to quantify the halogen concentrations. Oxygen was used because of its similar concentrations in samples and standards. Fluorine and chlorine were calibrated using ATHO-G and T1-G glasses (for more details see Baker et al., 2022). External precision based upon reference material measurements was ±2.8% (n = 32) for F and ±1.0% (n = 16) for Cl; these values were propagated together with the within

Table 1
Sulfur and Halogen concentrations in nakhlite clinopyroxenes by SXRF (S and Cl) and by ion microprobe (F).

Analysis	Grain	Crystal	Spot	Location[1]	S (ppm)[2]	Cl (ppm)[2]	F (ppm)
MIL 03346							
47748		D1	1	Core	14	1 (dl)[3]	
47749		D1	2	Core	28	5	
47750		D1	4	Rim	16	1	
47751		D1	5	Rim	51	11	
47752		D1	6	Core	16	5	
Ion probe		D1	1i	Core		6	32
Ion probe		D1	2i	Rim		11	117
47731		D4	1	Core	32	0.3 (bdl)[4]	
Ion probe		D4	3i	Core		295	80
47732		D4	2	Rim	66	27	
Ion probe		D4	2i	Intermediate		6	73
Ion probe		D4	1i	Rim (near crack)		444	206
47745		D7	1	Core	11	4	
47746		D8	1	Core	12	3	
47747		D8	1	Core	14	10	
Nakhla							
47645	2	1	1	Rim	14	37	
47646	2	1	2	Core	11	24	
47647	2	1	3	Core	12	18	
Ion probe	2	1	2i	Core		3	84
Ion probe	2	1	3i	Core		3	63
Ion probe	2	1	1i	Rim		4	158
47648	2	1	4	Rim	14	23	
47643	2	2	1	Core	9	11	
47644	2	2	2	Core	9	10	
47654	4	1	1	Core	18	34	
47655	4	1	2	Core	14	12	
47656	4	1	3	Rim	9	12	
47657	4	1	4	Rim	15	14	
47649	6	1	1	Core	13	13	
47650	6	1	2	Core	9	13	
NWA 998							
47659		1–3	1	Core	9	19	
47660		1–3	2	Core	8	32	
47681		1–3	3	Low Mg# core	8	18	
47665		1–4	1	Core	8	22	
47666		1–4	2	Core	24	64	
47667		1–4	3	Rim	17	32	
47668		1–6	1	Rim	12	117	
47669		1–6	2	Rim	10	40	
47670		1–6	3	Core	11	15	
47671		1–6	4	Rim	15	17	
47672		1–6	5	Core	16	18	
47673		1–11	1	Rim	11	13	
47674		1–11	3	Core	24	18	
47677		1–12	1	Core	11	15	
47678		1–12	2	Core	12	15	
47679		1–12	3	Rim	16	49	

[1] Locations for SXRF analyses are shown in Appendix A. Supplementary Materials; locations for the ion probe analyses are shown in Figs. 4–6.
[2] S and Cl were analyzed by SXRF, F was analyzed by ion probe.
[3] The detection limit (dl) for S and Cl is ~1 ppm.
[4] This concentration is below the detection limit (bdl).

run uncertainty to yield an estimate of overall uncertainty on the concentration measurements (excluding uncertainty in the reference material concentrations). Based upon analyses of ultrapure silica Herasil® glass we estimate ~2 ppm F and a similar value for chlorine as our maximum background values. However, as discussed in Baker et al. (2022), Herasil® glass is not considered nominally Cl-free, and use of this glass as a background monitor must be done carefully until concentrations of F and Cl in this glass are certified.

3. Results

Due to beamtime limitations only four to five crystals from each meteorite were chosen for point analyses of S, Cl, and F, and two clinopyroxene crystals, D1 and D4, from MIL 03346 and one crystal from Nakhla, clinopyroxene 2-1, were chosen for S and Cl mapping. All mapped crystals were chosen due to their size, so that a single map would cover a significant portion of the crystal, including the core, the annular mantle around the core, and the rim, in the time available for analysis. These crystals were chosen to be representative based upon petrographic observations, back-scattered electron imagery (BSE), and major element analyses that were similar to previously published analyses of clinopyroxenes in these meteorites, as shown by the wollastonite-enstatite-ferrosilite compositions in Fig. 2 (see Appendix A. Supplementary Material for complete analyses). None of the analyzed crystals were spatially associated with altered mesostasis and therefore unlikely to have been highly deformed due to the low-temperature shock documented by Daly et al. (2019). Furthermore, petrographic and SEM observations of the analyzed crystals revealed no evidence of deformation, undulose extinction, or recrystallization into smaller grains indicative of high shock pressures.

The crystal-mesostasis interfaces and cracks within crystals of the mapped clinopyroxenes of MIL 03346 and Nakhla were carefully investigated by SEM to search for S-rich and Cl-rich minerals indicative of post-magmatic alteration. Backscattered images and EDS analyses of

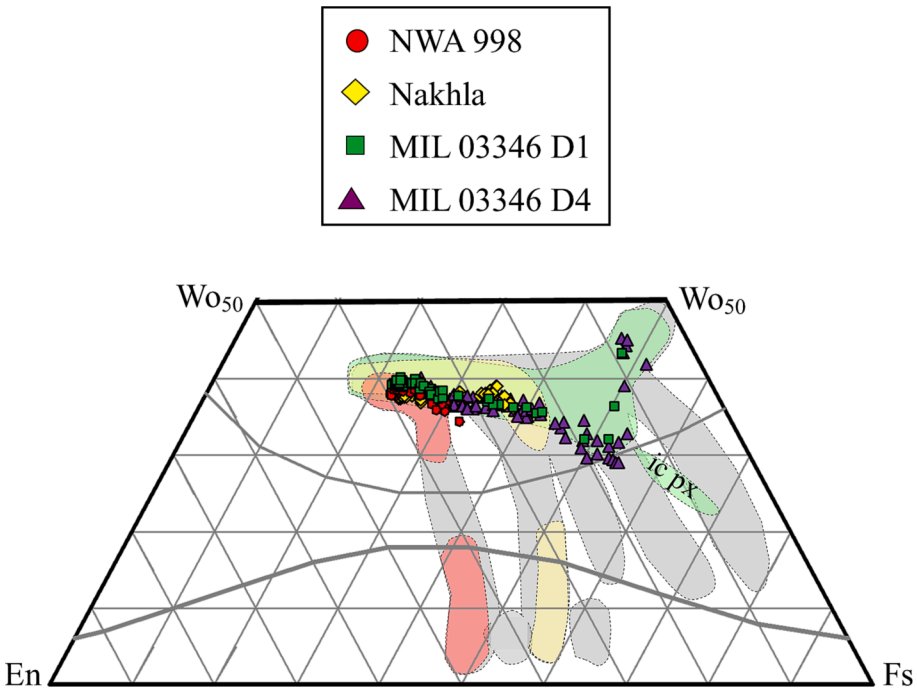

Fig. 2. Pyroxene quadrilateral with compositions of crystals from MIL 03346 (green squares and purple triangles), Nakhla (yellow diamonds), and NWA 998 (red circles). The clinopyroxene compositions of each meteorite are similar to previously published clinopyroxenes from the same meteorites shaded in red for NWA 998, yellow for Nakhla, and green for MIL 03346. The abbreviation "ic px" indicates intercumulus pyroxene in MIL 03346 (Day et al., 2006). Also plotted in gray are the compositional fields for clinopyroxenes in other nakhlites (see: Sautter et al., 2002; Mikouchi et al., 2003; Treiman, 2005; Beck et al., 2006; Day et al., 2006; Imae and Ikeda, 2007; Treiman and Irving, 2008; Jambon et al., 2016; Balta et al., 2017; Udry and Day 2018).

these samples indicate only rare, apparently magmatic sulfides in the mesostasis at the boundaries of the mapped clinopyroxenes. Instead, the small, mesostasis crystals found at the edges of the clinopyroxenes were most commonly iron–titanium oxides and phosphates. Furthermore, no S-rich crystals were found in the cracks cutting the clinopyroxenes. Despite our petrographic, SEM, and electron microprobe investigations that found no alteration in the crystals to be analyzed for S, Cl, and F, some analyses of these elements yielded results far above those expected for magmatic systems and may be due to some alteration (discussed in more detail below and in the Appendix A. Supplementary Material).

3.1. *Point analyses of sulfur, fluorine, and chlorine concentrations*

The sulfur and chlorine concentrations were measured in 4 crystals from MIL 03346, 4 from Nakhla, and 5 from NWA 998. The S and Cl concentrations in nakhlite clinopyroxenes vary from 4 to 63 ppm and from the detection limit of 1 ppm up to 65 ppm, respectively (Table 1, Fig. 3). Volatile concentrations from different points within the core of the same clinopyroxene are often, but not always, near-or-within uncertainty of each other, whereas analyses taken in different locations of the rim of the same clinopyroxene often show highly variable concentrations (Fig. 3).

Under conditions of either equilibrium or fractional crystallization in a closed system, and in the absence of the stabilization of another phase rich in either S (e.g., a melt, fluid, or crystal) or Cl (e.g., apatite, amphibole, halite or fluid), crystal rims would be expected to be enriched in these volatile elements compared to the cores. Rims are generally enriched in S and Cl relative to the cores, but there are some exceptions (Fig. 3).

3.1.1. *Clinopyroxene cores*

3.1.1.1. MIL 03346. The clinopyroxenes in MIL 03346 display S concentrations from 14 to 32 ppm and Cl from below the detection limit to 10 ppm (Table 1, Fig. 3a). As discussed in Section 3.2, mapping of D1 and D4 clinopyroxene cores provides a clearer picture of the volatile evolution. Clinopyroxenes in MIL 03346 have core compositions from approximately $Wo_{40}En_{38}Fs_{22}$ to $Wo_{39}En_{36}Fs_{25}$ or Mg#, MgO/(FeO + MgO), of 60–66 and demonstrate the greatest extent of major element zoning from core to rim (Figs. 2, 4, and 5).

Ion microprobe analyses of the cores of crystal D1 and D4 in MIL 03346 gave F concentrations of 32 (D1) and 72 ppm (D4). The chlorine concentrations measured by ion microprobe in cores from both crystals were 6 ppm, consistent with the SXRF results. In both crystals, we performed additional analyses that appear to have been located on apparently altered regions because the chlorine concentration was 444 ppm and fluorine was 206 ppm, neither of which we think represents the concentration in the crystal during its magmatic growth, but instead are most probably indicative of later alteration (cf., e.g., Treiman, 2005; Sautter et al., 2006; McCubbin et al., 2009; Stopar et al., 2013; Giesting and Filiberto, 2016; Udry and Day, 2018; Daly et al., 2019), which was however not visible petrographically, in backscattered electron imagery, or in the electron microprobe analyses.

3.1.1.2. Nakhla. Nakhla clinopyroxene cores display a positive correlation between S and Cl (Table 1, Fig. 3b), with a slope of 1.9 and a correlation coefficient of 0.56. However, two core analyses of clinopyroxene 4-1 differ significantly in Cl; one contains 12 ppm, whereas the other has 33 ppm. Nevertheless, the observed correlation provides putative evidence that during crystallization of Nakhla clinopyroxene cores, no S or Cl was removed from the melt by formation of other S- or Cl-rich phases. The observed trend may be the product of closed system crystallization (White, 2013). This Nakhla trend from Fig. 3b falls far from the MIL 03346 core compositions in Fig. 3a, providing additional support for the different petrogenetic histories of Nakhla and MIL 03346 (cf., Day et al., 2006; Udry and Day, 2018). Two ion microprobe analyses of the Nakhla crystal 2-1 core both yielded 3 ppm Cl and F concentrations of 84 and 63 ppm. The Cl concentrations measured by ion microprobe are one-fourth the concentration of Cl in the two points analyzed by SXRF in this sample; we attribute these differences to heterogeneities in the core.

3.1.1.3. NWA 998. Most of the clinopyroxene cores in NWA 998 display S concentrations (8–24 ppm) within the range defined by Nakhla and MIL 03346 and with Cl concentrations near 20 ppm, although two exceptional core analyses of 32 ppm (1–11) and 64 ppm (1–4) chlorine were found. The crystal core 1–4 from NWA 998 was analyzed in two

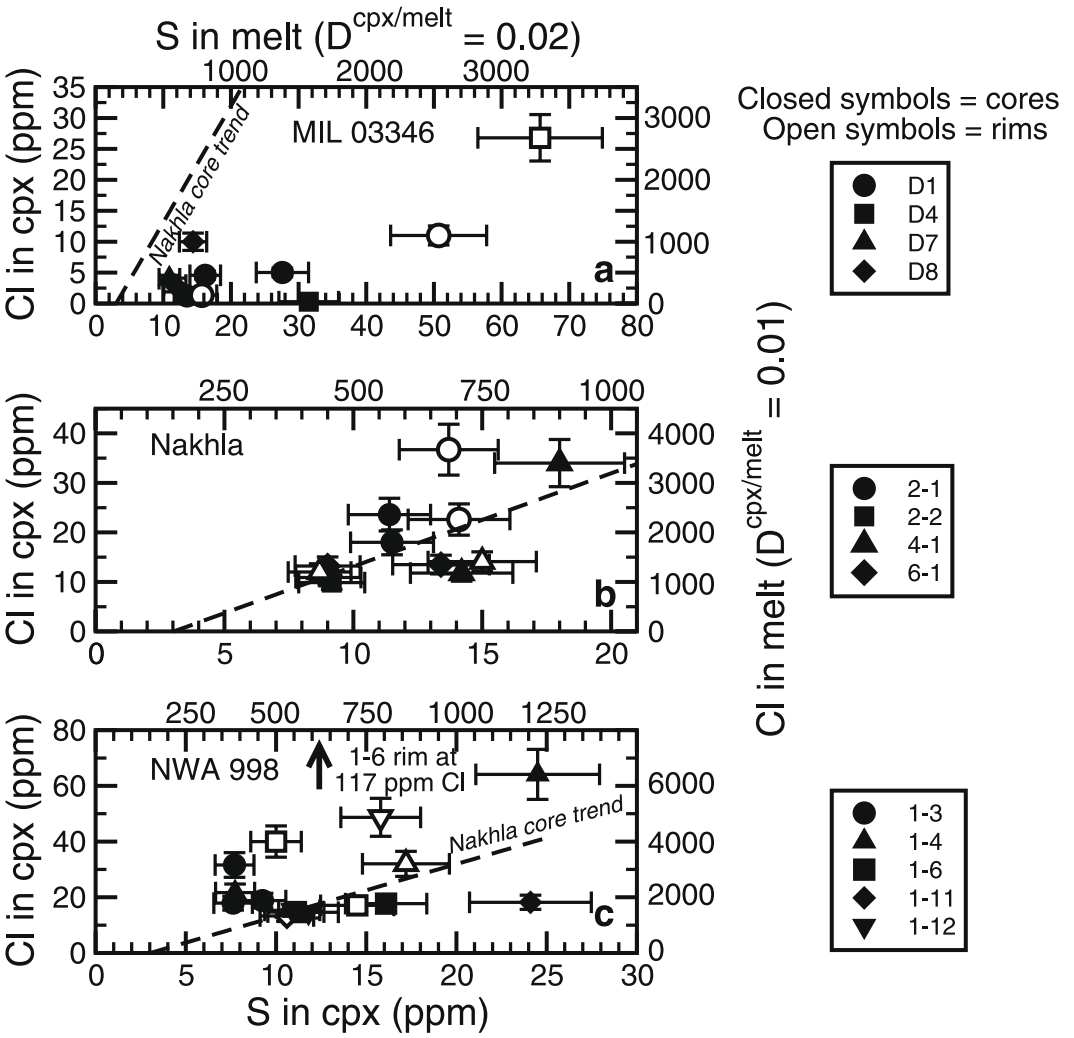

Fig. 3. Point analyses of S and Cl in clinopyroxenes analyzed by SXRF. (a) MIL 03346. (b) Nakhla. (c) NWA 998. Filled symbols depict analyses of cores, and open symbols of the same shape as used for the core represent analyses of the same crystal's rim. Each panel displays the measured concentrations of S (lower axis) and Cl (left-hand axis) in the clinopyroxene. The concentrations of the volatiles in corresponding melts are calculated using the partition coefficients shown in the Fig. and plotted on the upper axis (S) and right-hand axis (Cl) in each panel.

points, one contained 25 ppm S and 64 ppm Cl, and the other 8 ppm S and 22 ppm Cl (Fig. 3c). The Nakhla core trend (Fig. 3b) passes close to many of the NWA 998 core compositions (Fig. 3c), suggesting that fractional crystallization may be dominantly responsible for the compositional variations seen in the clinopyroxene cores of NWA 998 and supporting previously seen similarities in NWA 998 and Nakhla (Udry and Day, 2018). The major element compositions of the NWA 998 crystals only display a small variation, approximately $Wo_{39}En_{39}Fs_{22}$ to $Wo_{38}En_{36}Fs_{26}$ and Mg# 62–66 (Fig. 2, Udry and Day, 2018), similar to clinopyroxene cores in Nakhla, $Wo_{38}En_{39}Fs_{23}$ to $Wo_{39}En_{35}Fs_{26}$ (Fig. 2, Udry and Day, 2018; see also Fig. 2) or Mg# of 61–63.

3.1.2. Clinopyroxene rims

3.1.2.1. MIL 03346. The SXRF analyses of S and Cl in the rim of clinopyroxene D1 in MIL 03346 are very different from one another (Fig. 3a). One of them plots at low concentrations of S and Cl (16 and 1 ppm, respectively) and within uncertainty of 2 of the 3 core analyses of the crystal, whereas the other rim is significantly enriched in S (50 ppm) and Cl (12 ppm). The rim of clinopyroxene D4 is even more enriched in S (~64 ppm) and Cl (27 ppm); this degree of enrichment is particularly intriguing because the core analysis of D4 has a Cl concentration below the detection limit. These two crystals show remarkable zoning of the major element concentrations in their rims, where at an approximately constant Fs_{50} the wollastonite component increases from Wo_{30} to Wo_{45} with the Mg# falling to 15 (cf., Day et al., 2006; Udry and Day, 2018). The clinopyroxene rims also display an increase in the concentration of Fe^{3+}, as indicated by Mössbauer data (Domeneghetti et al., 2013) and calculated from the stoichiometry (Appendix A. Supplementary Material).

3.1.2.2. Nakhla. The rims of the Nakhla clinopyroxene 2-1 (Fig. 3b) are slightly enriched in S (14 ppm) compared to the core (12 ppm). The Cl concentration in one rim is similar to the core analyses (~22 ppm), but the other rim is significantly enriched (38 ppm). The two rim analyses of Nakhla clinopyroxene 4-1 contain similar Cl concentrations (~12 and 14 ppm Cl) and S concentrations (~9 and 15 ppm), which bracket the core S concentration of this crystal (Fig. 3b). Nakhla clinopyroxene rims are significantly enriched in FeO compared to the cores, with ferrosilite concentrations reaching Fs_{42} or Mg# of 37 (Fig. 2), but they are generally less depleted in En and less enriched in Wo than MIL 03346 clinopyroxene rims.

3.1.2.3. NWA 998. Two of the NWA 998 clinopyroxenes display rims that are lower in both S and Cl than the cores (1–6, 1–11), as shown in Fig. 3c. Both the core and rim of clinopyroxene 1–11 contain similar Cl

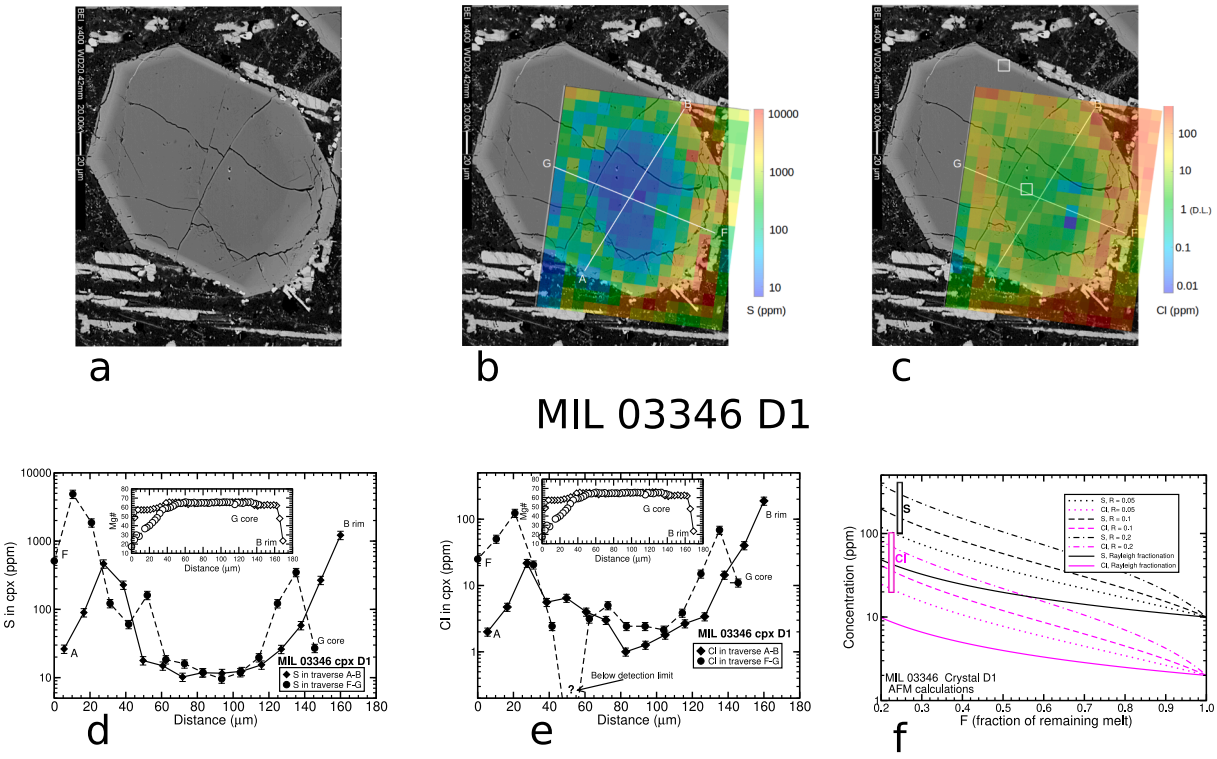

Fig. 4. Maps and traverses of MIL 03346 D1. (a) Backscattered electron image of analyzed crystal. The minerals at the contact between the crystal and the mesostasis are dominantly iron–titanium oxides with less-abundant sulfides. (b) Sulfur map with traverse locations marked by lines. (c) Chlorine map with traverse locations marked by lines. Ion probe analyses for Cl and F are marked by open squares; analysis D1 1i is near the center, and D1 2i is in the upper left on the rim. (d) Sulfur concentrations along traverses marked in b and c; inset displays Mg#, Mg/(Mg + Fe), along traverses. (e) Chlorine concentrations along traverses marked in b and c; inset displays Mg#, Mg/(Mg + Fe), along traverses. (f) Concentrations of S (black) and Cl (magenta) in the crystal during assimilation of regolith, fractional crystallization, and mixing (AFM) calculated using the model of DePaolo (1981) compared to the range of concentrations of S and Cl. The rate of assimilation to crystallization, R, used was 0.05–0.2. Also shown are the trajectories for Rayleigh fractionation during crystal growth of S (black) and Cl (magenta). Concentrations of S (black) and Cl (magenta) in unaltered clinopyroxene near the crystal rims are shown as the boxes in this panel that are located at the average fraction of mesostasis present in MIL 03346. Please see text for more details.

concentrations (~15 and 12 ppm, respectively), but the S concentration of the core is 24 ppm and the rim contains only 11 ppm. The rim and core analyses of clinopyroxene 1–6 are similar, with ~15 ppm S and 20 ppm Cl (Fig. 3c). The rim analysis of 1–6 with 15 ppm S and 116 ppm Cl (Fig. 3c) is very Cl-rich compared to other clinopyroxene rims analyzed in this study. The core compositions of clinopyroxene 1–4 bracket the rim composition. Only clinopyroxene 1–12 clearly demonstrates a rim enriched in Cl (~45 ppm) compared to its core (~18 ppm), whereas the S concentrations in the core and in the rim are within uncertainty of each other. The major element compositions of NWA 998 clinopyroxenes display moderate iron enrichments up to Fs_{33} (Fig. 2) and Mg# of 51 in the rims.

The inter- and intra-crystalline variations of S and Cl in the nakhlites' clinopyroxenes support a complex petrogenetic history of the three meteorites investigated, although some of the variation seen within an individual crystal may be due to complex zoning in clinopyroxene (cf., Skulski et al., 1994; Watson, 1996). In most cases the core-to-rim variations of S and Cl in the point analyses do not provide unambiguous evidence of enrichment of residual melts in S and Cl during crystallization. However, the clearest evidence for S- and Cl- enrichment is seen for MIL 03346 clinopyroxenes.

3.2. Maps of sulfur and chlorine in 3 clinopyroxenes

Portions of crystals D1 (Fig. 4) and D4 (Fig. 5) from MIL 03346 and crystal 2-1 from Nakhla (Fig. 6) were mapped by SXRF. These maps allow us to better understand the zoning of Cl and S during clinopyroxene growth in the samples studied, particularly MIL 03346.

3.2.1. Crystal D1 in MIL 03346

Approximately one-half of crystal D1 in MIL 03346 was mapped (Fig. 4). The map confirms the heterogeneous concentrations of S and Cl displayed in the point analyses (Fig. 3a) and demonstrates zoning from the center of the map to its edges, which on some edges of the map correspond to the crystal/mesostasis boundary and on other edges of the map are inside the crystal (Fig. 4b). The map demonstrates a general, positive, correlation between S and Cl.

The map displays a core that is apparently displaced from the center of the crystal with S concentrations of 10–15 ppm (Fig. 4b, d) and Cl concentrations of 1–5 ppm (Fig. 4c, e), similar to the point analyses of this crystal's core (Fig. 3a). The asymmetry in the map may reflect crystallographically controlled, or sector, zoning (Paquette and Reeder, 1990; Skulski et al., 1994; Watson, 1996), and its upper right-hand edge (Fig. 4a-c) corresponds to a visible change in the gray-scale level of the BSE image. Surrounding the core is a mantle of approximately 30 μm in width, in which both S and Cl concentrations increase. Near traverse ends A and F (Fig. 4d, e) the sulfur concentrations reach values between 1000 and 10000 ppm (or 0.1 and 1 wt%) and those of Cl reach 100 ppm. The correlation of the S and Cl maps with the major element electron microprobe traverses (Fig. 4d, e) and backscattered electron images (Fig. 4a) demonstrate that the annular mantle enriched in volatiles corresponds to the regions in the crystal where the Mg# decreases (Fig. 4d, e). Regions displaying a lower Mg# are often associated with increasing concentrations of Ti, Al, and stoichiometrically calculated Fe^{3+} in the clinopyroxene (Appendix A. Supplementary Material). Closer to the rim, near points A and F, both the S and Cl concentrations drop to lower values; near location A the concentrations of S and Cl are

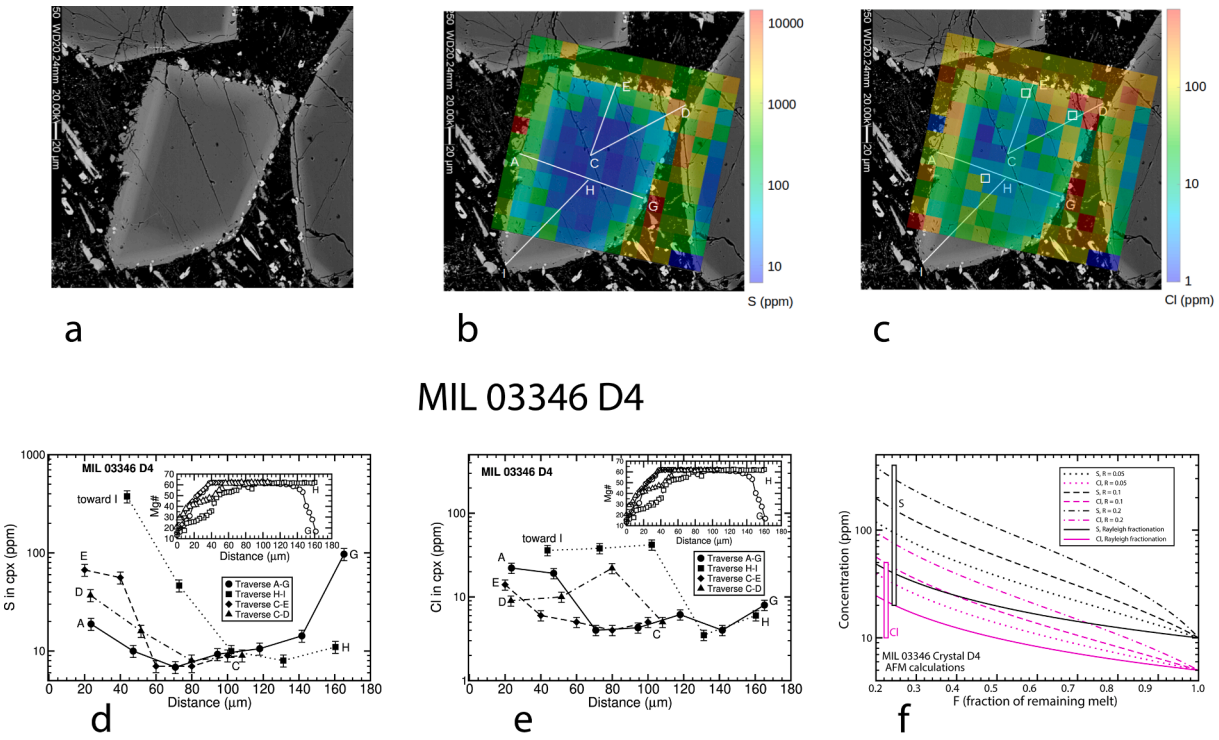

Fig. 5. Maps and traverses of MIL 03346 D4. (a) Backscattered electron image of analyzed crystal. (b) Sulfur map with traverse locations marked by lines. The minerals at the contact between the crystal and the mesostasis are dominantly iron-titantium oxides and less-abundant sulfides. (c) Chlorine map with traverse locations marked by lines. Ion probe analyses for Cl and F are marked by open squares; analysis D4 1i is in the top center, D4 2i is in the upper right, and D4 3i is near the center. (d) Sulfur concentrations along traverses marked in b and c; inset displays Mg#, Mg/(Mg + Fe), along traverses. (e) Chlorine concentrations along traverses marked in b and c; inset displays Mg#, Mg/(Mg + Fe), along traverses. (f) Concentrations of S (black) and Cl (magenta) in the crystal during assimilation of regolith, fractional crystallization, and mixing (AFM) calculated using the model of DePaolo (1981) compared to the range of concentrations of S (black) and Cl (magenta) near the crystal rims. The rate of assimilation to crystallization, R, used was 0.05–0.2. Also shown are the trajectories for Rayleigh fractionation during crystal growth of S (black) and Cl (magenta). Concentrations of S (black) and Cl (magenta) in unaltered clinopyroxene near the crystal rims are shown as the boxes in this panel that are located at the average fraction of mesostasis present in MIL 03346. Please see text for more details.

similar to those of the core. The edges on the right-hand side of the crystal in Fig. 4 are all enriched in both S and Cl, which may be due to inadvertent analysis of a mixture of the crystal and the mesostasis, which contains Fe-Ti oxides, sulfides, and possibly secondary sulfates (Day et al., 2006; Hallis and Taylor, 2011; Stopar et al., 2013), at the clinopyroxene-mesostasis interface.

The maps show regions that are either anomalously enriched or depleted in S or Cl. Some of the extremely enriched regions appear associated with cracks in the crystals, whereas others (e.g., those in the upper left-hand corner of the map) are not. Other regions are anomalously low (e.g., the concentration of Cl at one point along the G–F profile is below the detection limit). The association of some enriched points with cracks suggests that the volatile concentrations at those points in the map do not represent the equilibrium volatiles in the crystal at magmatic temperatures and may be due to subsolidus alteration and possibly formation of sulfates (Day et al., 2006; Hallis and Taylor, 2011; McCubbin et al., 2013). We cannot *a priori* eliminate post-magmatic alteration of crystals along those cracks, either on Mars, during the impact that launched MIL 03346 into space, or weathering on Earth and will discuss these possibilities in Section 4.3 and in Appendix A. Supplementary Material.

3.2.2. Crystal D4 in MIL 03346

Almost the entire exposed surface of crystal D4 in MIL 03346 was mapped (Fig. 5). The crystal displays a core with approximately 10 ppm S (Fig. 5d) and 5 ppm Cl (Fig. 5e). The core Cl concentration in the map is significantly higher than the single spot analysis of crystal D4 (which is below the detection limit), and the sulfur analyses in the map are significantly lower than the single point analysis (Fig. 3a), although some points along the traverse H-I are similar to the point analysis (Fig. 5d, e). Surrounding the core is a mantle enriched in both S and Cl, whose location corresponds to changes in the Mg#, Ti, Al, and stoichiometrically calculated Fe^{3+} (Appendix A. Supplementary Material), similar to what is seen for crystal D1. However, unlike D1, there is no clear drop in either S or Cl close to the crystal rim.

The D4 map includes more of the mesostasis than the map of D1 and demonstrates that with the exception of a few enriched regions, the mesostasis contains between 100–1000 ppm S and 10–100 ppm Cl. The map also includes a small fraction of neighboring clinopyroxene crystals and demonstrates that their rims are of similar compositions to D4 and that the core of the crystal on the right in the image is also similar to D4.

3.2.3. Crystal 2-1 in Nakhla

The mapped Nakhla crystal, 2-1, appears to have a heterogeneous core that may be partially resorbed and contains small, iron-rich inner zones along the A–B and D–L traverses, which are lighter-gray in the BSE image (Fig. 6a) and have major element concentrations similar to the rim; previous observations of Fe-rich regions within Nakhla clinopyroxenes were reported by Treiman (2005). Unlike crystals in MIL 03346, this clinopyroxene is surrounded by other crystals of clinopyroxene and plagioclase on most of its edges, but small blebs of glass are found at points A, B and L (Fig. 6a, b). The S concentration in the darker, Mg-rich, portion of the core is between ~6 and 10 ppm, however near the Fe-rich portion of the core along the A-B traverse the S concentration drops to ~2 ppm. The Cl concentration of the core is much more variable. Although large portions of the core contain ~10–20 ppm Cl, the iron-rich core regions and regions near some cracks contain ~100 ppm Cl (Fig. 6b, c). Although enrichment in both S and Cl can be seen near some

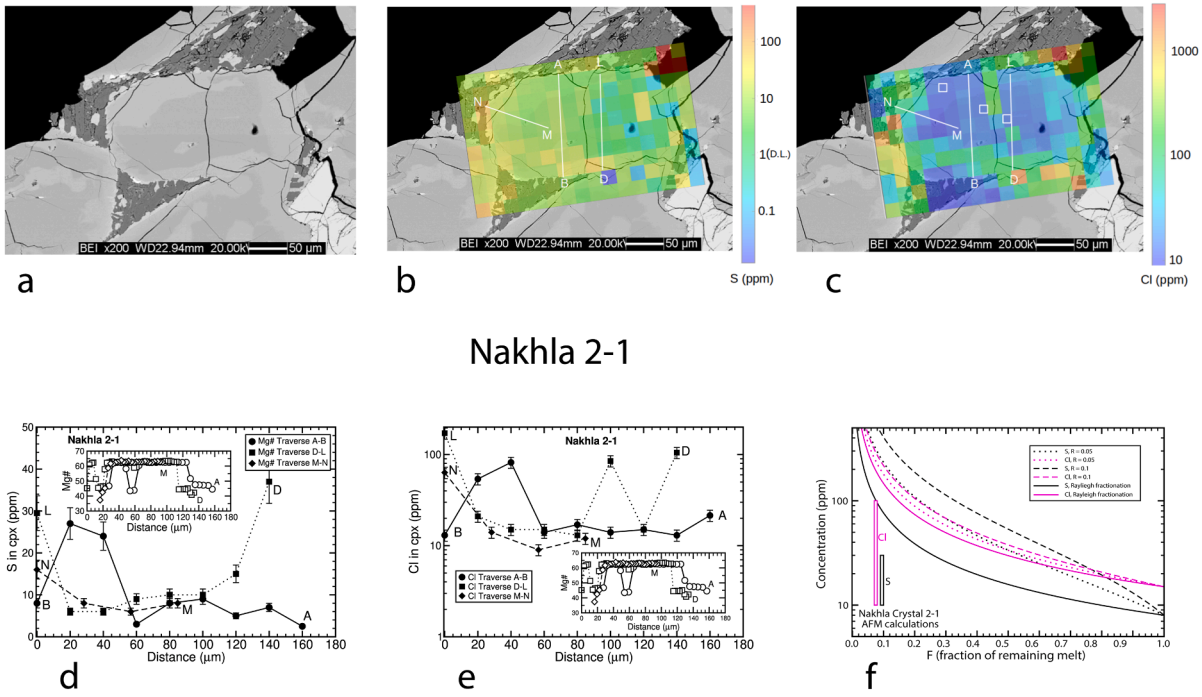

Fig. 6. Maps and traverses of Nakhla 2-1. (a) Backscattered electron image of analyzed crystal and the surrounding clinopyroxene crystals and groundmass. The groundmass minerals near the contact with the mapped crystal are dominated by iron–titanium oxides and a calcium phosphate mineral (possibly apatite); a few sulfide minerals are also present. (b) Sulfur map with traverse locations marked by lines. (c) Chlorine map with traverse locations marked by lines. Ion probe analyses for Cl and F are marked by open squares; analysis 2-1 1i is near the upper left-hand side of the crystal, 2-1 2i is in the center near the D-L traverse, and 2-1 3i is between them. (d) Sulfur concentrations along traverses marked in b and c; inset displays Mg#, Mg/(Mg + Fe), along traverses. (e) Chlorine concentrations along traverses marked in b and c; inset displays Mg#, Mg/(Mg + Fe), along traverses. (f) Concentrations of S (black) and Cl (magenta) in the crystal during assimilation of regolith, fractional crystallization, and mixing (AFM) calculated using the model of DePaolo (1981) compared to the range of concentrations of S and Cl (boxes) near the crystal rims. Also shown are the trajectories for Rayleigh fractionation during crystal growth of S (black) and Cl (magenta). The rate of assimilation to crystallization, R, used was 0.05 and 0.1. Concentrations of S (black) and Cl (magenta) in unaltered clinopyroxene near the crystal rims are shown as the boxes in this panel that are located at the average fraction of mesostasis present in Nakhla, 9% (Udry and Day, 2018). Please see text for more details.

rims of the crystals, the zoning of S, and particularly of Cl, are not as evident as in the MIL 03346 crystals. Interestingly, the A–B traverse shows low S and Cl near the A-end of the traverse, but higher concentrations near the Fe-rich region in the core of the crystal, although there is a drop in both S and Cl at B (Fig. 6d, e). The other two traverses, D–L and M–N demonstrate enrichment of S and Cl near crystal boundaries, although the D–L traverse is complicated by a singular, high Cl concentration in the iron-rich portion of the crystal core, whose chlorine concentration is similar to those seen in the iron-rich rims.

4. Discussion

4.1. Geological setting and genetic relations of nakhlites on Mars

Nakhlites are generally accepted to be samples of one or more shallow intrusions or cumulate portions of lava flows (e.g., Lentz et al., 1999, 2011; Day et al., 2006; McCubbin et al., 2013; Udry and Day, 2018) whose light rare-earth enriched parental magmas were formed by melting of a long-term, incompatible element depleted mantle source (see Udry and Day, 2018, and references therein). The varying amounts of mesostasis (Day et al., 2006; Udry et al., 2012; Corrigan et al., 2015; Udry and Day, 2018), the meteorite textures (Hammer, 2009: Udry and Day, 2018), zoning of Fe, Mg, and Ca in olivine (Mikouchi and Miyamoto, 2002; Mikouchi et al., 2003), and zonation of lithium, both concentration and isotopic, and magnesium and iron in clinopyroxenes (Richter et al., 2016) have been used to assess each meteorite's cooling history and from these data the proximity to a cooling boundary (such as the martian surface or the martian shallow crust) was inferred.

Of the meteorites studied, MIL 03346 contains the greatest fraction of mesostasis, ~24% (Udry et al., 2012), and some authors place this meteorite at a cooling boundary near the top of a flow or intrusion. Based upon the fraction of mesostasis and crystal size distributions, Nakhla is placed in the top to the middle of a flow or intrusion (Udry and Day, 2018), and NWA 998 was placed in the proximity of another cooling boundary, but one that was possibly warmer than the one near MIL 03346 and therefore inferred to be near the base of a flow (Udry and Day, 2018). Unlike some earlier studies that hypothesized nakhlites were from a single lava flow, similar to the terrestrial analogue Theo's flow in Ontario, Canada (e.g., Lentz et al., 1999, 2011; Day et al., 2006), Udry and Day (2018) used trace element signatures to propose that MIL 03346 was in one flow, or flow lobe, and Nakhla and NWA 998 were in another, or possibly two other flows or flow lobes. Despite these complexities, Udry and Day (2018) concluded that nakhlites "share strong co-genetic petrogenetic traits much the same as terrestrial lava-sill-dike complexes."

The shared co-genetic traits of nakhlites suggest the possibility that the petrogenetic history of nakhlites can be better understood through combination of the results of this work and previously published analyses of nakhlites. We are most interested in the history of sulfur and chlorine in these rocks as the results discussed above demonstrate complexities that may not be explicable by simple crystallization fractionation; the first step in investigating the nakhlite petrogenetic history is to determine the temperature and pressure at which the nakhlite clinopyroxenes crystallized.

4.2. Temperatures and pressures of clinopyroxene crystallization

We determined the crystallization conditions of nakhlites by clinopyroxene-melt geothermobarometry (Lessel and Putirka, 2015; Neave and Putirka, 2017), using our analyses of clinopyroxene core

compositions (e.g., Fig. 2). Because nakhlites are cumulate rocks, the liquid composition from which they crystallized can only be estimated. Proposed parental liquids for nakhlites previously were estimated to be subalkaline basaltic melts (with some variability) from analysis of melt inclusions (many of them crystallized) in nakhlite clinopyroxene and olivine (e.g., Harvey and McSween, 1992; Varela et al., 2001; Stockstill et al., 2005; Imae and Ikeda, 2007; Sautter et al., 2012; Goodrich et al., 2013). We used the various published parental liquid compositions and our major element analyses of clinopyroxene core compositions in MIL 03346, Nakhla, and NWA 998 to calculate pressures and temperatures of clinopyroxene crystallization using the clinopyroxene-melt geothermobarometers of Neave and Putirka (2017) and Lessel and Putirka (2015), the latter specifically calibrated for martian bulk compositions. We note that estimated temperatures and pressures have considerable uncertainties, which are a combination of those intrinsic to the geothermobarometers (on the order of 50 °C and 140 MPa; Neave and Putirka, 2017) and the compositional range of the estimated parental melts.

Both geothermobarometers produced similar crystallization temperatures for the clinopyroxene cores. We obtained temperatures from 843 to 1197 °C with an average of 1061 ± 109 °C (uncertainty is 1 standard deviation) for the Lessel and Putirka (2015) model and an average of 1075 ± 90 °C for the Neave and Putirka (2017) model. The highest estimated temperature (which is within approximately 1 standard deviation of the mean) is similar to the experimentally determined maximum temperature of clinopyroxene stability in Longhi and Pan's (1989) proposed Nakhla parental liquid, ~1215 °C, and to the estimated temperature of clinopyroxene crystallization obtained using another proposed parental melt composition, ~1170 °C (Sautter et al., 2012). A slightly lower temperature for augite crystallization in a nakhlite parental melt comes from the experimental results of Imae and Ikeda (2008) on their proposed parental melt, ~1150 °C. Therefore, the cores of the clinopyroxenes in the studied nakhlites probably crystallized between ~1150 and 1215 °C.

Both geothermobarometers produced negative average crystallization pressures for the clinopyroxene cores (−120 ± 310 MPa for Lessel and Putirka, 2015; −730 ± 990 MPa for Neave and Putirka, 2017). Negative pressures are suggestive of disequilibrium between the clinopyroxene cores and the proposed parental liquids. However, if we only consider pressure calculations for calculated crystallization temperatures of 1150 °C and greater, the average pressures of crystallization are 300 ± 440 MPa (using Lessel and Putirka, 2015) and 370 ± 70 MPa (using Neave and Putirka, 2017). These average pressures imply that crystallization of the clinopyroxene cores in the studied nakhlites occurred at crustal depths (Semprich and Filiberto, 2020, Wieczorek et al., 2022), or on the surface of Mars. Applying the Ti/Al geobarometer of Nekvasil et al. (2007) to our samples produces similar results (430–930 MPa, upper- to mid-crustal pressures; Appendix A. Supplementary Material) to those found by Peslier et al. (2019) on a suite of other nakhlite samples including the meteorites studied here.

Pairing mesostasis compositions of MIL 03346 (Imae and Ikeda, 2007; Jambon et al., 2016) with our analyses of the clinopyroxene rims yields average calculated rim crystallization conditions of 1014 ± 27 °C, 740 ± 160 MPa (using Lessel and Putirka, 2015) and 987 ± 32 °C, 300 ± 390 MPa (using Neave and Putirka, 2017). The mean temperatures are within 1-sigma of each other and are approximately 150 °C lower than the best-estimate core crystallization temperatures. An overall slow, post-crystallization cooling rate of the MIL 03346 magma was inferred from the low closure temperature (Tc ~ 500 °C) obtained from the Fe^{2+}-Mg degree of order and intracrystalline cation site distribution in MIL 03346 clinopyroxene cores (Domeneghetti et al., 2013). Based on these data and on the petrographic evidence indicating the quench of interstitial melt at high temperature, Domeneghetti et al. (2013) suggested that after a fast cooling rate at high temperature the magma experienced a much slower cooling rate at lower temperature, consistent with the hypothesis of repeated emplacement of magma in a thick cooling sill or with subsequent emplacement of additional lava flows on the top of the nakhlite pile (Domeneghetti et al., 2013). The pressure of 740 MPa calculated by the Lessel and Putirka (2015) model is surprisingly higher than those estimated for the core and appears rather implausible. The pressure estimates obtained following the approach of Neave and Putirka (2017) imply a simpler crystallization model, where the rims formed at pressures similar to the cores or, considering the large standard deviation, closer to the surface. Crystallization of nakhlite clinopyroxene rims at near-surface pressures has previously been advocated by many researchers based upon the meteorites' textures, replacement of olivine by orthopyroxene, and cooling rate calculations based upon isotopic and chemical zonation in phenocrysts (e.g., Lentz et al., 1999; Treiman, 2005; Day et al., 2006; Richter et al., 2016; Udry and Day, 2018).

In summary, our preferred interpretation of the geothermobarometry calculations is that the cores of the nakhlite clinopyroxenes crystallized in upper-to-mid-level crustal magma chambers at temperatures between 1150 and 1215 °C. These clinopyroxenes were then transported to near-surface, or surface, conditions where cooling and rim growth occurred; for the case of MIL 03346 this temperature appears to have been approximately 1000 °C. The final igneous episode involved cooling of the individual nakhlites at different depths within lava flows or near-surface intrusions.

4.3. *Are measured volatile concentrations in clinopyroxene due to magmatic or post-magmatic processes?*

The post-magmatic histories of these meteorites are complex and involve interactions with high- and low-temperature hydrothermal fluids (e.g., Bridges and Grady, 1999, 2000; Day et al., 2006; Sautter et al., 2006: McCubbin et al., 2009; Changela and Bridges, 2011; Hallis and Taylor, 2011; Bridges and Schwenzer, 2012; Filiberto et al., 2014; Giesting and Filiberto, 2016), the impact that launched the meteorites off the surface of Mars, the ~11 Ma transit from Mars to Earth (Korochantseva et al., 2011; Cohen et al., 2017), and weathering on Earth's surface (e.g., Treiman, 2005; Day et al., 2006; Hallis and Taylor, 2011; Peslier et al., 2019). Although potentially each of these events could have affected the concentrations of S, Cl, and F in the clinopyroxenes, all evidence points towards the dominant control of magmatic processes on the elemental concentrations and distributions measured in this study. However, some of the high concentrations of volatiles (e.g., 117 ppm Cl in the rim of NWA 998 crystal 1–6) in the clinopyroxenes may be due to non-magmatic (e.g., alteration) processes. Following Peslier et al. (2019) we evaluated the possible alteration of the clinopyroxenes by impacts on Mars, hydrothermal systems, and terrestrial weathering; the details are provided in the Appendix A. Supplementary Material and only a summary is presented here.

Peslier et al. (2019) investigated the influence of impacts on the water concentration and D/H ratios of nakhlite clinopyroxenes and found that impacts had little effect. Because of the higher diffusivity of hydrogen in comparison to sulfur and chlorine in silicate melts (e.g., Baker and Balcone-Boissard, 2009) and therefore probably in clinopyroxene crystals, the evidence and arguments used by Peslier et al. (2019) indicate that the distributions of S and Cl seen in the nakhlite clinopyroxenes should not have been significantly altered by impact processes.

The possible effects of hydrothermal alteration was modeled using diffusion of Cl at 200 and 700 °C (Appendix A: Supplementary Material) in an amphibole because no Cl diffusion measurements in clinopyroxene were found (we consider amphibole to be the best analogue for Cl diffusion in clinopyroxene because of their similar structures), and the results indicate that alteration should occur only within about 10 μm of a surface in contact with a Cl-rich fluid at low temperatures, which is similar to the widths of Cl-enriched zones near some cracks in the mapped clinopyroxenes (Figs. 4–6). At high temperatures diffusive modification of Cl in clinopyroxene is much more extensive. However

the dissolution rate of these minerals into hot water is so rapid (Zhang et al., 2013) that we would expect to see dissolution features in the investigated clinopyroxenes, but none were found. Based upon these diffusion calculations and our observations we conclude that high- or low-temperature alteration of the Cl concentrations in the clinopyroxenes was minor.

No studies on the diffusion of S in clinopyroxene or amphibole were found, but the observation that sulfur diffusivities are below those of chlorine in silicate melts (e.g., Baker and Balcone-Boissard, 2009) suggests that any alteration of sulfur concentrations by hydrothermal systems should be spatially limited to distances similar to those estimated for chlorine.

Although most nakhlites are finds and have experienced weathering on Earth (e.g., Treiman, 2005; Hallis and Taylor, 2011), Peslier et al. (2019) demonstrated little evidence of terrestrial alteration in their samples of the same meteorites investigated in this study and demonstrated that they could interpret their water concentrations and δD ratios by magmatic degassing and crystallization. Carraro et al. (2010) studied total hydrogen in clinopyroxene crystal cores by Elastic Recoil Detection Analysis from the same three nakhlites samples investigated here. They only detected small amounts of terrestrial hydrogen contamination along cracks, providing further support for the lack of significant terrestrial alteration.

Thus, sulfur and chlorine analyses of the clinopyroxenes more than approximately 10 μm away from cracks appear to be magmatic signatures and can be used to investigate the evolution of the nakhlite magmatic system.

4.4. Sulfur, chlorine, and fluorine in nakhlite parental melts

The point analyses of S and Cl in clinopyroxene cores (Fig. 3) demonstrate sulfur concentrations varying from 8 to 32 ppm and Cl concentrations from below the detection limit to 65 ppm, with the majority of points showing sulfur and chlorine concentrations between 10 and 20 ppm. The maps of clinopyroxenes D1 and D4 in MIL 03346, as well as clinopyroxene 2-1 in Nakhla (Figs. 4–6), demonstrate that these three clinopyroxene cores all contain approximately 13 ppm sulfur. The chlorine concentrations in the cores of MIL 03346 are more variable, but typically contain ~5 ppm, whereas the core of Nakhla clinopyroxene 2-1 and NWA 998 clinopyroxenes are more enriched in Cl, containing ~17 ppm.

We can estimate the S, Cl and F concentrations in the melts from which the cores crystallized using the sulfur partition coefficients of Callegaro et al. (2020) and the fluorine and chlorine partition coefficients of Baker et al. (2022). Both sets of partition coefficients were measured on terrestrial basaltic melt compositions and clinopyroxenes that crystallized from them. The compositions of proposed nakhlite parental melts (e.g., Goodrich et al., 2013) and nakhlite clinopyroxenes are different from those in the partitioning experiments, notably higher in total iron, but no clinopyroxene/liquid partition coefficients of S, Cl, and F have been measured in martian magmatic compositions. The compositional differences between terrestrial and martian magmas may influence the partition coefficients, however Righter et al. (2009) demonstrated that sulfide saturation in both martian and terrestrial basalt melts can be described by a single relationship, and Filiberto and Dasgupta (2011) demonstrated that the Fe/Mg exchange coefficient between martian basaltic melts and olivines was only approximately 17% above the same value for terrestrial basaltic melts. Therefore, although we acknowledge possible differences in the partitioning behavior of S, Cl, and F in terrestrial and in martian magmatic systems, all available evidence indicates that they will be small.

We apply a sulfur clinopyroxene-liquid partition coefficient of 0.02, based upon partition coefficients determined using the same SXRF analytical techniques (Callegaro et al., 2020) as applied in this study. For Cl, we use a partition coefficient of 0.01 (Baker et al., 2022). However, as stressed by Baker et al. (2022) the chlorine concentrations in their experimentally produced clinopyroxenes are near, or at, the detection limit of the ion microprobe and their partition coefficient may be a maximum. Nevertheless, this Cl partition coefficient of Baker et al. (2022) is similar to previously measured ones by Dalou et al. (2012, 2014). Although problems may arise when applying a partition coefficient determined by ion microprobe (Baker et al., 2022) to Cl concentrations measured by SXRF, the similarity of Cl concentrations in MIL 03346 determined by ion microprobe to those determined by SXRF suggests that those problems are minimal. We use a fluorine partition coefficient of 0.2, determined by ion microprobe (Baker et al., 2022). We note that this value is a little greater than those measured by Dalou et al. (2012, 2014), ~0.075–0.15.

Fig. 3 explicitly converts the concentrations of S and Cl in the clinopyroxenes into S and Cl concentrations in the liquids from which the cores crystallized; these values range from ~200 to 1600 ppm S and ~250 to 6500 ppm Cl. These calculated variations in the concentrations of S and Cl in the melt may be due to local enrichment or depletion of sulfur and chlorine in the residual liquid during clinopyroxene crystallization. The variations also may be related to crystallographic controls on trace element partitioning (e.g., Paquette and Reeder, 1990; Skulski et al., 1994; Watson, 1996). Because of these possibilities it is useful to consider the mean concentrations of volatiles in the clinopyroxene cores and those calculated in the corresponding liquids.

The average of the sulfur analyses of clinopyroxene cores in MIL 03346 (Fig. 3) and the 3 Cl analyses above the detection limit produces an average of 18 ± 8 ppm S and 5 ± 3 ppm Cl. The maps of the two crystals from MIL 03346 (Figs. 4 and 5) indicate that broad regions of the crystal cores can be characterized by S concentrations between ~7 and 15 ppm, a little lower than the average calculated from the point analyses. On the other hand, the maps indicate Cl concentrations in the core similar to the average of point analyses. The calculated volatile concentrations in the parental melt of MIL 03346 are 900 ± 400 ppm S and 500 ± 300 ppm Cl; these means and 1-sigma standard deviations are based upon all analyzes of the MIL 03346 clinopyroxene cores and span a large range due to the variability of the measured S and Cl concentrations. The calculated sulfur concentration in the parental melt is similar to that measured in a melt inclusion in MIL 03346 by Imae and Ikeda (2007), 761 ppm S.

Converting the mean sulfur concentration of the Nakhla cores of 11 ± 4 ppm to a melt concentration yields 550 ± 200 ppm S; the same calculation for Cl in the cores, 15 ± 8 ppm, yields an average melt concentration of 1500 ± 800 ppm Cl. The S and Cl concentrations in the core of the mapped Nakhla clinopyroxene (Fig. 6) are quite similar to the averages of the point analyses (Fig. 3), with the exception of one anomalously Cl-enriched point on the D–L traverse that correlates with a lighter-gray (higher iron and lower Mg#) region of the clinopyroxene core.

The average S in the NWA 998 clinopyroxene cores is 13 ± 6 ppm and the average Cl is 24 ± 15 ppm; these values yield melt concentrations of 650 ± 300 ppm S and 2400 ± 1500 ppm Cl. If the two most S- and Cl-enriched NWA 998 core analyses (1–4 and 1–11) are not used, the S average in the crystal cores decreases to 10 ± 3 ppm and Cl to 19 ± 6 ppm, or average melt concentrations of 500 ± 150 ppm S and 1900 ± 600 ppm Cl.

The average core concentrations of S and Cl together with the elemental maps indicate that the melts from which MIL 03346, Nakhla, and NWA 998 crystallized contained similar concentrations of S (~500–900 ppm), but different mean concentrations of Cl (~500 ± 300 ppm in MIL 03346, ~1500 ± 800 ppm in Nakhla and ~1900 ± 600 ppm for NWA 998).

Considering the uncertainties in the calculated concentrations of S and Cl, the similarity of the volatile concentrations in the Nakhla and NWA 998 parental melts suggests that a single parental melt may be responsible for their clinopyroxene cores (cf., Udry and Day, 2018). The observation that the Nakhla trend in Fig. 3b is similar to the trend in core compositions of NWA 998 (Fig. 3c) also supports the hypothesis of a

single parental melt, or similar parental melts, for both meteorites. If a single parental melt produced both meteorites, then the higher Mg# of the clinopyroxene cores in NWA 998 than in Nakhla (Udry and Day, 2018; this study) suggests earlier crystallization of NWA 998 crystals.

The few, exploratory analyses of fluorine in crystal cores of MIL 03346 and Nakhla can also be used to estimate the F concentration in the parental melts. The low F concentration measured in crystal D1 of MIL 03346, 32 ppm, yields a melt concentration of 160 ppm, whereas the higher concentration, 72 ppm, indicates a melt with 360 ppm F. The two Nakhla measurements, 84 and 63 ppm, indicate parental melts with 420 or 315 ppm F. The significant enrichment of Cl to F in the parental melts is consistent with findings that most nakhlite apatites crystallized from a melt with more chlorine than fluorine (e.g., McCubbin et al., 2013, 2016).

McCubbin et al. (2013) and Udry and Day (2018) presented evidence for a genetic relationship between nakhlites and chassignites. McCubbin et al. (2016) used measurements of F and Cl in apatite from chassignite NWA 2737 to estimate the Cl:F ratio in the parental melt and found a ratio of 2.6–3.5. Combining our mean concentrations of Cl in the parental melt of MIL 03346 with the two F analyses we made yields Cl:F ratios of 1.4 and 3.1 in the parental melt. Performing the same calculation for Nakhla yields Cl:F ratios of 4.5 and 6.0. We note that whereas only one of our values falls within the range of that determined by McCubbin et al. (2016) for NWA 2737, all of the values in the two studies are not dissimilar and support a genetic relationship between chassignites and nakhlites.

4.5. Comparison of sulfur, chlorine, and fluorine concentrations between nakhlite and shergottite parental melts

Volatile concentrations estimated in nakhlite parental melts can be compared to those in parental shergottite melts (Usui et al., 2012; McCubbin et al., 2016; Paquet et al., 2021). Usui et al. (2012) measured S, Cl, and F concentrations in melt inclusions trapped in olivine from shergottites Yamato 980459 (incompatible element depleted), and Larkman Nunatak 06319 (incompatible element enriched). Three melt inclusions in Yamato 980459 showed a mean of 822 ± 163 ppm S, 38 ± 11 ppm Cl, and 14 ± 4 ppm F, whereas one melt inclusion in Larkman Nunatak 06319 yielded 82 ppm S, 1018 ppm Cl and 490 ppm F (Usui et al., 2012). The high concentration of sulfur found in the Yamato 980459 melt inclusions is similar to our estimates of sulfur (~500 ppm) in the nakhlite parental melts. In contrast, the melt inclusions are significantly depleted in Cl and F compared to our estimates for nakhlite melts. On the other hand, the Larkman Nunatak 06319 melt inclusion is significantly depleted in S compared to our estimate, but the Cl and F concentrations are similar to those estimated from our clinopyroxene analyses.

McCubbin et al. (2016) used measured concentrations of F and Cl in apatites from the enriched basaltic shergottite Shergotty and the depleted basaltic shergottite QUE 94201 combined with bulk meteorite analyses of Filiberto et al. (2016) to estimate the concentrations of volatiles in the parental melts. They determined that the parental melt to Shergotty contained 36 ppm F and 116 to 155 ppm Cl. For QUE 94201 the authors proposed volatile concentrations in the parental melt based upon their measurements and the olivine-hosted melt inclusion in Yamato 980459 (Usui et al., 2012) that were significantly lower: 10 ppm F and 16–21 ppm Cl. These concentrations are similar to those measured in melt inclusions of Yamato 980459 (Usui et al., 2012) and less than we determined for the nahklite parental melts.

Paquet et al. (2021) used the concentrations of highly siderophile elements in 16 shergottites to calculate the concentrations of sulfur in shergottite parental melts. Shergottites enriched in lithophile trace elements and with high $^{187}Os/^{188}Os$ and $^{87}Sr/^{86}Sr$ were estimated to be formed by 25–30% fractional crystallization of a melt with 250 ± 50 ppm S, whereas shergottites with lower lithophile trace element abundances and isotopic ratios were formed by 10–15% fractionation from a parental melt with 350 ± 100 ppm S (Paquet et al., 2021). These sulfur concentrations are lower than our estimate of nakhlite parental melts (~500 ppm), but they are in the range of the lowest parental melt concentrations for both Nakhla and NWA 998 (Fig. 3). These low concentrations of sulfur in both nakhlite and shergottite parental melts provide evidence that the mantle source regions of these martian meteorite parental magmas are not extraordinarily enriched in sulfur.

4.6. Sulfur, chlorine and fluorine in primitive melts and the nakhlite source region

The melts that crystallized nakhlites are not considered to be primary mantle melts because their Mg# values are too low; the nakhlite parental melts must have evolved from primary melts, presumably by crystallization of ferromagnesian phase(s) (Treiman, 2005, and references therein; Udry and Day, 2018). Because sulfur and halogens are more incompatible in olivine and orthopyroxene than in clinopyroxene (Callegaro et al., 2020), these volatile concentrations should increase in residual melts with crystallization, and primary melts from the martian mantle are expected to contain less sulfur and halogens than the nakhlite parental melt concentrations calculated above.

The amount of fractionation necessary to produce a nakhlite parental melt from a primary melt of a martian peridotite can be calculated from the Mg# of the clinopyroxene cores and the Mg# of primary martian mantle melts. The Mg# of the cores, ~0.64, is combined with a $K_D^{Fe/Mg}{}_{(cpx/melt)}$, or $(Fe/Mg)^{cpx}/(Fe/Mg)^{melt}$, of 0.23 (Goodrich et al., 2013) to calculate a nakhlite parental melt with an Mg# of 0.29. This Mg# is similar to that of many of the previously proposed nakhlite parental melts (cf., Goodrich et al., 2013). Bertka and Holloway (1994) estimated that near-solidus martian primary mantle melts have an Mg# of 0.48 and that at low pressures olivine will be the dominant crystallizing phase. Following Bertka and Holloway (1994), we start with their primary melt composition JFR-4 and fractionate 1% spinel + clinopyroxene and then 18% olivine. The residual melt has an Mg# of 0.29, but not the correct CaO/Al_2O_3 ratio to be a nakhlite parent, as previously stressed by Bertka and Holloway (1994). Using mass balance for all volatile species and crystal/melt partition coefficients, the concentrations of S, Cl, and F were calculated in the primary melt. The sulfur partition coefficients of olivine ($D_s = 0.001$) and of clinopyroxene ($D_S = 0.02$) are from Callegaro et al. (2020). Similarly, the partition coefficients of Baker et al. (2022) were used for Cl and F; the D_{Cl} for olivine was set to 0.003 and for clinopyroxene to 0.01. The D_F for olivine was 0.003 and for clinopyroxene was 0.235. The partition coefficients of S, Cl, and F for spinel are assumed equal to those of olivine because of their similar structure with short cation-oxygen bond lengths (see discussion in Callegaro et al., 2020 for effects of bond lengths and mineral structure on sulfur partitioning). With these values we correct the ~500 ppm S in nakhlite parent melts and the lowest calculated concentrations of Cl, ~400 ppm, and F, 160 ppm (for MIL 03346), to predict a primary melt with ~400 ppm S, ~320 ppm Cl, and ~130 ppm F.

The concentrations of sulfur, chlorine, and fluorine in the martian mantle source of nakhlites can be calculated from the fraction of mantle melted to produce the primary melts and the partitioning of the volatiles between crystals and melt. Martian primary melts were probably produced by 5–30% partial melting of the martian mantle (Longhi and Pan, 1989; Bertka and Holloway, 1994; Treiman, 2005; Filiberto and Dasgupta, 2011; Matsukage et al., 2013; Wang and Becker, 2017; Udry and Day, 2018). In addition to the partition coefficients for olivine, spinel, and clinopyroxene used above for the calculation of the primary melt, we used a value of $D_S = 0.001$ for orthopyroxene (Callegaro et al., 2020) and for garnet, where the partition coefficients of S, Cl, and F for garnet are assumed equal to those of olivine because they are both orthosilicates with short cation-oxygen bond lengths (Callegaro et al., 2020). Similarly, the partition coefficients of Baker et al. (2022) were used for Cl and F. The D_{Cl} for orthopyroxene and garnet was set to 0.003. The mineralogy of the source used to calculate the bulk partition coefficient

is based upon the experiments of Bertka and Fei (1997) at 20 and 30 kbar and is 0.59 olivine, 0.19 orthopyroxene, 0.15 clinopyroxene, and 0.07 garnet. All calculations assumed that only these phases were present and that any phases enriched in sulfur and/or halogens (e.g., sulfide, apatite, amphibole) were completely consumed at the solidus and played no role in controlling the concentrations of S, F, and Cl in the melt. The calculated bulk crystal/melt distribution coefficient for this model is 0.004 for both sulfur and chlorine, and 0.08 for fluorine. Possible source region concentrations of S, Cl and F were calculated for both equilibrium and aggregate fractional fusion (modal melting) models (Shaw, 1970).

The calculated concentrations of S, Cl, and F in the source region are between ~15 to ~120 ppm; both the equilibrium and aggregated fractional melting models yield similar concentrations (Fig. 7). If the primary melts were produced by 5% melting of the source region, then that region would contain ~20 ppm S, ~16 ppm Cl, and ~15 ppm F, whereas in the case of 30% melting the source region would contain ~120 ppm S, ~97 ppm Cl, and F concentrations of either 48 (equilibrium melting) or 40 ppm (aggregate fractional fusion). Using the highest estimated concentration of Cl in the NWA 998 parental melt would increase the chlorine concentration in the source by a factor of 3.5 and using the highest concentration of F in Nakhla would increase the source concentration by 2.5*x*.

The nakhlite source region appears enriched in fluorine and probably in chlorine in comparison to shergottite source regions. Based upon previously published analyses of melt inclusions or apatites in three shergottites (Yamato 980459, QUE 94201, and Shergotty), Filiberto et al. (2019) estimated the concentrations of F and Cl in these meteorites' source regions. The source regions of Yamato 980459 and QUE 94201 had between 1 and 1.6 ppm F, whereas the source region of Shergotty contained 3.6–5.4 ppm F (Filiberto et al., 2019). Even this highest estimate for the Shergotty source region is only ~1/3 the minimum fluorine concentration we calculate for the nakhlite source. The calculated concentration of Cl in the Yamato 980459 and QUE 94201 source regions was between 1.6 and 4.2 ppm (Filiberto et al., 2019), and the source region of the Tissint shergottite was calculated to contain 1.2 ppm Cl (Clay et al., 2020), far below the minimum of ~15 ppm of Cl (for 5% melting) we calculate for the nakhlite source region. On the other hand, the Shergotty source region is calculated to contain between 12 and 23 ppm Cl (Filiberto et al., 2019) and overlaps with our minimum estimate.

Table 2 compares our estimates of the concentrations of S, Cl, and F in the nakhlite source region to previous estimates of these elements' concentrations in the bulk silicate portion of Mars. Fig. 8 schematically summarizes our calculations of the sulfur and halogen concentrations in the nakhlites' parental melt, in the primary melt from mantle melting, and in the mantle source. The mantle source concentrations of Cl and F are very similar to those of the bulk silicate Mars calculated by many other researchers, and the best match occurs for melt fractions between 10 and 20% (Table 2, Fig. 7).

Previous estimates of sulfur in the bulk silicate portion (or mantle) of Mars vary from 86 ppm to 2000 ppm (Table 2). Our calculations of sulfur in the nakhlite source region are consistent with the lowest concentrations in Table 2 (Lodders and Fegley, 1997; Steenstra and van Westrenen, 2018). The low S concentration in the nakhlite source can either be interpreted as evidence for a low-S mantle on Mars, or that the nakhlite source region is depleted in S relative to the prevalent martian mantle, possibly by crust formation.

Long-term depletion of the nakhlite source region, supported by our calculated low S concentrations, has been put forward by previous researchers using major elements (e.g., Longhi and Pan, 1989), trace element ratios, and isotopic signatures (Treiman, 2005; Udry and Day, 2018). Conversely, our calculated concentrations of Cl and F in the nakhlite source region are similar to the bulk silicate Mars values, implying that these two elements avoided depletion, or were perhaps enriched after an earlier depletion event and prior to melting of the nakhlite source. These characteristics of the nakhlite source are intriguing and may provide important information on the mantle evolution of Mars, including metasomatism (Day et al., 2018; Udry et al., 2020), but that needs to be investigated in future research.

Interestingly, our results imply that the nakhlite source region has sulfur concentrations a little below that of the depleted MORB source on Earth as determined by multiple researchers: Salters and Stracke (2004): 119 ppm; Nielsen et al. (2014): 195 ± 45 ppm; Ding and Dasgupta (2017): 100–200 ppm; and Sun et al. (2020): 120 to 300 ppm with an average of 206 ± 25 ppm. The estimated nakhlite source region Cl concentrations are higher than either Earth's primitive or depleted mantle, where estimates of chlorine in the depleted terrestrial mantle vary from 0.51 to 7.3 ppm and in the primitive terrestrial mantle from

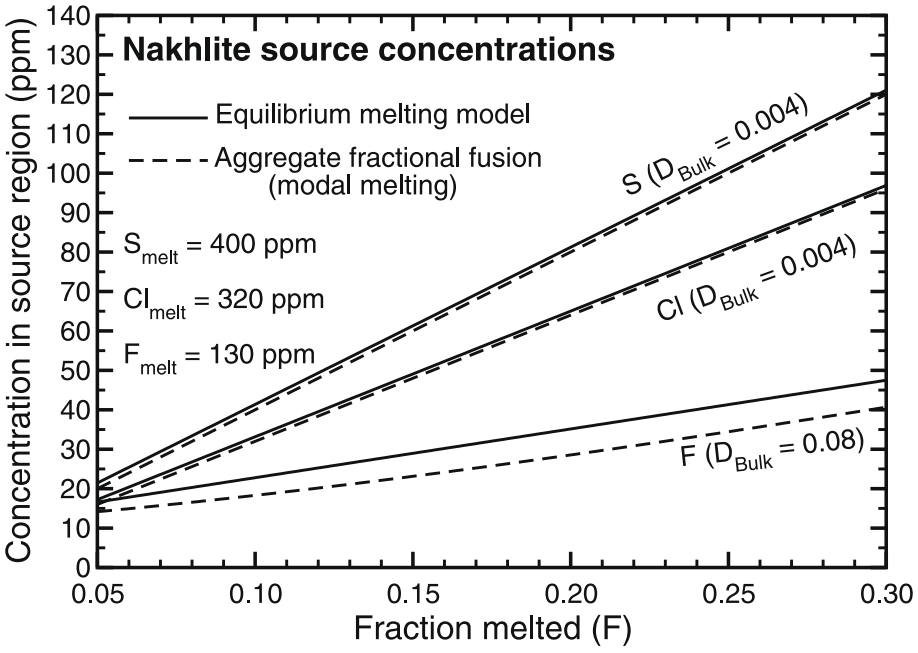

Fig. 7. Calculated concentrations of S, Cl, and F in the nakhlite source region as a function of the martian mantle melt fraction necessary to produce the primitive melts that undergo crystallization and give rise to nakhlite parental melts. Please see the text for details of the calculations.

Table 2
Concentrations of S, Cl and F in the nakhlite source region and bulk silicate Mars.

	Nakhlite source	Bulk Silicate Mars								
	This work	D & W[a]	L & F[b]	Gaillard et al.[c]	Taylor[d]	Ding et al.[e]	Filiberto et al.[f]	S & v W[g]	Y & M[h]	Clay et al.[i]
Sulfur	20–120	–	110	700–2000		700–1000		86–276	360 ± 120	
Chlorine	16–97	38	150		32 ± 9		25 ± 8		28	22
Fluorine	14–48	32	41		21 ± 13		25 ± 13		30	

[a] Dreibus and Wänke (1987), Wänke and Dreibus (1988).
[b] Lodders and Fegley (1997).
[c] Gaillard et al. (2013).
[d] Taylor (2013).
[e] Ding et al. (2015).
[f] Filiberto et al. (2016).
[g] Steenstra and van Westrenen (2018).
[h] Yoshizaki and McDonough (2020), sulfur from Wang and Becker (2017).
[i] Clay et al. (2020).

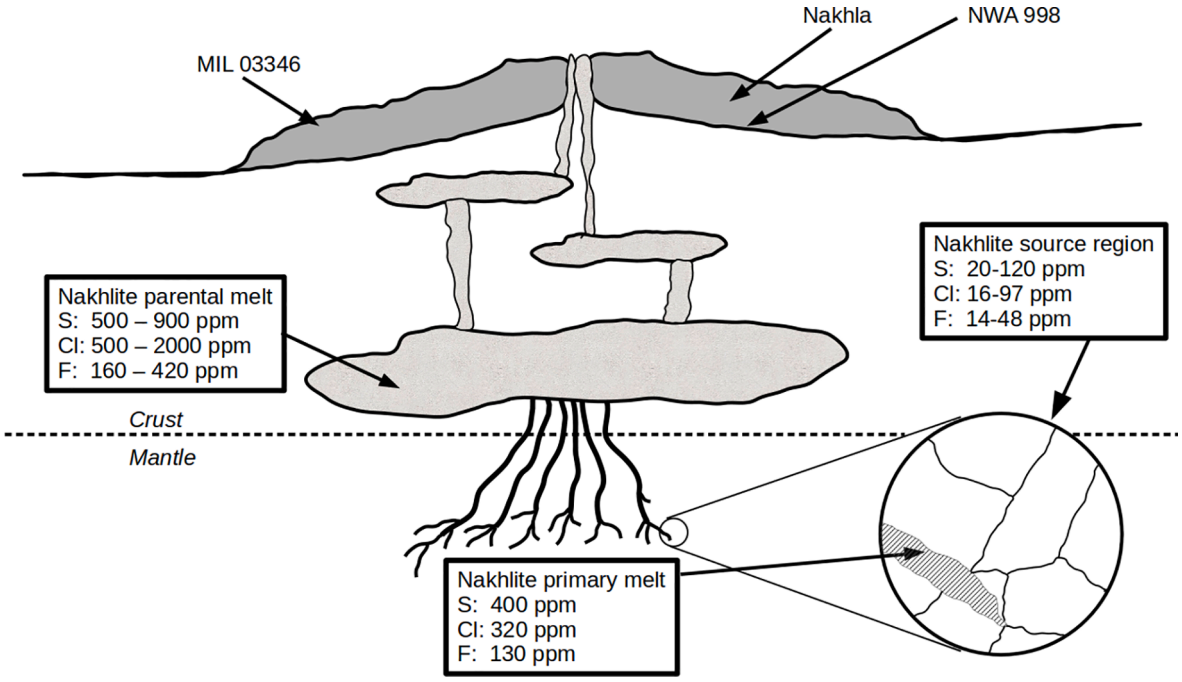

Fig. 8. Schematic cartoon of the calculated sulfur, chlorine and fluorine concentrations in nakhlite source regions and magmas (not to scale!) as discussed in the text. The range of concentrations for the nakhlite parental melt is shown, but only the minimum concentrations for the nakhlite primary melt are given. The range of volatile concentrations in the nakhlite source is calculated from the primary melt composition for a range of melt fractions from 0.05 to 0.30 (or 5–30% melting), which results the range of volatile concentrations in the source displayed. Uncertainties in the calculations are discussed in the text.

1.4 to 30 ppm (Frezzotti and Ferrando, 2018). On the other hand, our estimates of F in the nakhlite source region are similar to those of Earth's depleted, 11–65 ppm, and primitive mantle, 18–25 ppm (Frezzotti and Ferrando, 2018).

4.7. Sulfur and chlorine zoning in nakhlite clinopyroxenes: A history of volatile enrichment followed by degassing

The sulfur and chlorine concentrations in the studied clinopyroxenes increase from the cores outward toward the rims of the crystals. This zoning is best seen in the maps and traverses of the MIL 03346 crystals (Figs. 4 and 5), but can also be discerned in the map of the Nakhla crystal (Fig. 6) and in the general tendency of the S and Cl concentrations in many point analyses of clinopyroxene rims to be volatile-enriched compared to their corresponding cores (Fig. 3). Furthermore, S and Cl concentrations in crystal D1 of MIL 03346 are depleted close to one of the rims, suggestive of volatile loss during the latest stages of clinopyroxene growth (Fig. 4).

The zoning profiles for MIL 03346 crystals demonstrate that areas closer to the rim (or the mantle around the core) commonly can be enriched in S by 10–40× in crystal D1 and 5–10× in crystal D4 (Figs. 4 and 5), although some analyses suggest enrichment up to a factor of 500. Most of the analyzed map outside the core of crystal D1 has a maximum Cl enrichment of ~10× (Fig. 4), although there is evidence of extreme chlorine enrichment to ~100×. Crystal D4 displays chlorine enrichments reaching only about 10× (Fig. 5). As discussed above, some of the most extreme enrichments seen in the profiles (e.g., 5000 ppm S along the G–F traverse) are associated with cracks in the crystal where high- and low-temperature hydrothermal alteration or terrestrial weathering may have occurred (Day et al., 2006; Sautter et al., 2006; McCubbin et al., 2009; Hallis and Taylor, 2011, Stopar et al., 2013; Giesting and Filiberto, 2016; Bridges and Schwenzer, 2012).

Applying the same partition coefficients as used above (Fig. 3) indicates crystallization of the clinopyroxene rims from melts with extremely high sulfur and chlorine concentrations. For example, 1000 ppm S in the crystal suggests 5 wt% S in the melt. Such concentrations

are far above the sulfur concentration at sulfide saturation (SCSS) of approximately 1600 ppm (Righter et al., 2009; see Appendix A. Supplementary Material) and suggest the possibility of oxidized conditions such that much of the sulfur is in the 6+ state in the melt. More oxidizing conditions during clinopyroxene rim growth is consistent with greater amounts of stoichiometrically calculated Fe^{3+} in the rims than in the cores (Appendix A. Supplementary Material), although other processes may also be affecting the ferric iron in the clinopyroxene rims. Even assuming all sulfur was oxidized, a concentration of 5 wt% S in the estimated residual melts of MIL 03346 far exceeds the concentrations needed to saturate the system in anhydrite (calculated using the model of Baker and Moretti, 2011), and the magmatic, sulfur-bearing minerals in nakhlites are sulfides, not sulfates, in the mesostasis (Treiman, 2005). We suspect the high sulfur concentrations seen in the crystal rims may be due to the entrapment of sub-micrometer scale sulfides in the clinopyroxenes that were not visible using our imaging techniques, or to subsolidus alteration by hydrothermal fluids. Alternatively the discrepancy between extremely high calculated concentrations of sulfur in coexisting melts and the concentrations needed for either sulfide or sulfate saturation may be because simple partition coefficients for S are inapplicable at such high concentrations due to failure of S to follow Henry's law in either the melt, or the crystals, or both. Nevertheless, even ignoring the most extreme concentrations, the sulfur maps reflect increasing S concentrations in the melt during crystallization of the clinopyroxenes.

The maps also demonstrate increasing Cl concentrations in the melt during crystallization. A chlorine concentration of 200 ppm (rim B in crystal 03346 D1 and rims L and N in Nakhla 2-1) reflects a melt concentration of 2 wt% Cl. This concentration is similar to the maximum concentration of chlorine seen in terrestrial magmas of mafic to intermediate composition (Webster et al., 2018). High concentrations of chlorine in nakhlite melts are consistent with the presence of Cl-rich apatite in nakhlite melt inclusions and mesostasis (e.g., McCubbin et al., 2013), the discovery of a Cl-rich scapolite in a melt inclusion from Nakhla (Filiberto et al., 2014), and Sautter et al.'s (2006) observation of a Cl-amphibole in MIL 03346.

The zoning profiles for clinopyroxene 2-1 in Nakhla indicate enrichment in S by a factor of 2.5–4× and in Cl by a factor of up to 8× (Fig. 6). However, the zoning profiles in this crystal are more complicated because some are terminated at other crystals where enrichment is not expected, based upon prior studies that demonstrated no major-element zoning near crystal rims touching another crystal (cf., Treiman, 2005; Udry et al., 2020). However, iron- and volatile-rich regions are found in this crystal's core (Fig. 6) along the D-L traverse, the A–B traverse and at the crystal edges D, L and N.

The high concentrations of S and Cl in the MIL 03346 crystals far from cracks where hydrothermal alteration may have occurred cannot all be explained by enrichment in residual melts due to crystallization. Applying either a Rayleigh fractionation or equilibrium model for crystallization of the parental melt from which the clinopyroxene cores formed predicts that after 90% crystallization the residual melt would produce a clinopyroxene that is ~10× enriched in either S or Cl. Both Rayleigh fractionation or equilibrium crystallization models are capable of explaining much of the enrichment of S and Cl in the mapped Nakhla clinopyroxene, however the pattern of enrichment of these elements, particularly sulfur, close to the rim of clinopyroxenes in MIL 03346 significantly exceeds modeled predictions.

The enrichment in S and Cl in the MIL 03346 crystals also cannot be explained by the combination of rapid crystal growth and slow diffusion of S and Cl in the melts, the snowplow effect (Smith et al., 1955; Harrison and Watson, 1984). This process was modeled using Eq. (10) of Smith et al. (1955), the S and Cl partition coefficients in Fig. 3, and the diffusivities of S and Cl in a basaltic melt from Freda et al. (2005) and Alletti et al. (2007), respectively. These models demonstrate that over the range of expected clinopyroxene growth rates in basic magmas of 10^{-11}–10^{-8} m s^{-1} (Pontesilli et al., 2019; Bonechi et al., 2020; Giuliani et al., 2020) the Cl concentration would not exceed ~15 ppm at the clinopyroxene rim and the S concentration would not exceed ~35 ppm during the growth of the ~100 μm mantle and rim of the MIL 03346 clinopyroxenes studied. At the same growth conditions Nakhla clinopyroxene 2-1 could reach sulfur and chlorine concentrations of ~30 and ~40 ppm, respectively.

The chlorine and sulfur concentrations in melts and coexisting clinopyroxenes could be modified by formation of Cl- or S-rich phases. The crystallization of apatite, with high Cl concentrations and a low S partition coefficient (Konecke et al., 2017), is expected to limit the Cl enrichment in coexisting melts. However, the P_2O_5 concentrations estimated in the mesostasis (Imae and Ikeda, 2007; Jambon et al., 2016) are only ~1 wt% and imply that apatite saturation would occur only near the very end of crystallization of the nakhlite mesostasis (Watson, 1979). Formation of a liquid or solid sulfide phase with a high S partition coefficient and a low Cl partition coefficient would have the opposite effect, buffering the concentration of S in the melt. But MIL 03346 does not contain sulfide phenocrysts, only the mesostasis contains magmatic sulfide, indicating that sulfide saturation was reached late in its crystallization history. Hydrous fluids are expected to produce similar results to sulfides because the aqueous fluid/melt partition coefficient for sulfur in mafic-to-intermediate composition melts is >80 and of chlorine is less than 2 (Zajacz et al., 2012). However, any of these possible events would not substantially increase the concentration of both sulfur and chlorine in the melt, which is clearly seen in the MIL 03346 crystals D1 and D4; thus, another process must be occurring.

The enrichment of S and Cl near the rims of MIL 03346 crystals provides evidence of the assimilation of near-surface rocks and/or regolith rich in volatile elements. Assimilation of regolith was previously proposed due to the mass-independent fractionation of sulfur isotopes in nakhlites, indicating interaction between nakhlite magmas and sulfur processed in the martian atmosphere (Farquhar et al., 2000; Franz et al., 2014; Mari et al., 2019). Further evidence of assimilation was the discovery of Cl-rich amphibole in melt inclusions in augite (Sautter et al., 2006).

The composition of near-surface martian rocks and regolith is rich in oxidized sulfur and chlorine (Boynton et al., 2007; Morrison et al., 2018; Certini et al., 2020; Rampe et al., 2020). The sulfur and chlorine budget of Mars' rocks and regolith appears dominated by X-ray amorphous material, whose abundance varies from 14% to 71% (Morrison et al., 2018). The average concentrations of sulfur in these surface samples varies from 2.6 wt% in the bulk soil (Certini et al., 2020) to 6.45 wt% in the X-ray amorphous material in the soil (Morrison et al., 2018). The lowest average chlorine concentration is 0.7 wt% in the martian soil (Certini et al., 2020), and the highest is 2.9 wt% in the X-ray amorphous material of the Yellowknife Bay formation (Morrison et al., 2018). The concentrations of S and Cl in these martian surface materials are consistent with our hypothesis that the sulfur and chlorine concentrations of the clinopyroxene mantles in MIL 03346 are influenced by near-surface assimilation.

In order to further investigate the assimilation hypothesis we applied the assimilation-fractionation-mixing (AFM) model of DePaolo (1981) and compared its results to Rayleigh fractionation. The assimilant used in modeling was composed of 40% X-ray amorphous material, with S and Cl concentrations calculated as the average of the studies cited in the previous paragraph (Morrison et al., 2018; Certini et al., 2020; Rampe et al., 2020), and 60% of other materials (e.g., igneous, metamorphic, or sedimentary rocks) with negligible sulfur and chlorine concentrations, yielding an assimilant bulk concentration of 1.7 wt% S and 0.7 wt% Cl. The assimilation to crystallization rates, or R-values, in our model varied from 0.05 to 0.4. The clinopyroxene core compositions are assumed to have formed at the liquidus, a melt fraction (F) of 1, at which point assimilation began. These calculations are not expected to provide exact values of the R-values because we are ignorant of the exact composition of the potential assimilant, the timing of the assimilation in relation to each crystal's growth, and the limitations of the DePaolo (1981) model.

Nevertheless, this model provides a semi-quantitative means of comparing the effects of the AFM process and fractional crystallization on the S and Cl compositions of the clinopyroxenes.

Comparison of the AFM and Rayleigh fractionation models for MIL 03346 crystal D1 (Fig. 4e) demonstrates that AFM models with R values of 0.1–0.2 provide a much better fit to crystal rim compositions than Rayleigh fractionation because the latter cannot account for the high S and Cl concentrations detected in this crystal. The assimilation of sulfate-rich materials at, or near, the martian surface would lead to oxidation of the residual silicate melt and increase the SCSS, allowing the melt to reach higher sulfur concentrations (Baker and Moretti, 2011).

MIL 03346 crystal D4 (Fig. 5e) displays a range of S and Cl concentrations near its rims whose highest concentrations are best explained by the AFM model with R values similar to those for crystal D1 (Fig. 5e). However, the lowest values of S and Cl are consistent with Rayleigh fractionation (Fig. 5e). The differences seen between crystals D1 and D4 are attributed to the cumulate nature of this rock where the crystals may not have grown from exactly the same melt composition at the same time and were possibly accumulated into MIL 03346 after most of their growth was completed.

Modelling Nakhla crystal 2-1 indicates that Rayleigh fractionation better fits the S and Cl concentrations than the AFM models investigated (Fig. 6e). The lack of observable assimilation in this crystal is consistent with isotopic studies of other samples of this meteorite showing little-to-no evidence of mass-independent fractionation of sulfur isotopes (Franz et al., 2014; Mari et al., 2019). The different roles assimilation and Rayleigh fractionation played in the petrogenetic histories of MIL 03346 crystals and Nakhla crystal 2-1 provide further evidence that while these meteorites may come from the same igneous complex, they are not closely related (Day et al., 2006; Udry and Day, 2018).

Crystal D1 of MIL 03346 displays a drop in S and Cl near the crystal rim (Fig. 4). This drop may be attributed to the generation of a volatile phase into which S and Cl preferentially partition during the last stage of the crystal's growth. A similar drop is possibly evident in MIL 03346 D4 (Fig. 5), but not in Nakhla 2-1 (Fig. 6). The inferred location of Nakhla in the center of a flow or sill, as opposed to the location of MIL 03346 near the top (Udry and Day, 2018), may explain the lack of evidence for volatile loss in Nakhla 2-1, but the lack of unambiguous degassing evidence in MIL 03346 D4 remains enigmatic. Perhaps the crystallization of MIL 03346 D4 finished before volatile loss occurred or there was something in the local environment, at a scale below that of a thin section, that prevented volatile loss from the region of D4 but allowed degassing near D1.

5. Conclusions

Our findings on the sulfur, chlorine, and fluorine concentrations in nakhlite parental melts, primitive melts that fractionated to produce the parental melts, and the nakhlite source region of Mars are summarized in Fig. 8 and Table 2. These concentrations are similar to many previous estimates of sulfur and halogens in martian materials, although our estimate of the sulfur concentration in the nakhlite source region is lower than most previous estimates for the martian mantle, and chlorine concentrations are higher.

This study demonstrates that the measurement of volatiles in minerals from achondritic meteorites produced by igneous processes combined with partition coefficients between crystals and melts can be used to better understand the storage and transport of elements in meteorite parent bodies. However, maps of S and Cl in clinopyroxenes demonstrate the complex spatial distribution of these volatiles and that the effects of alteration by hydrothermal fluids in the studied meteorites must be carefully evaluated before using crystal compositions to determine magmatic histories. Analysis of such complex spatial distribution has, however, a large potential to address issues of magma contamination and degassing on the way from the mantle source to crustal emplacement. Our findings show that assimilation and degassing occurred for MIL 03346 meteorite, but these processes are not recorded in Nakhla nor in our spot analyses of clinopyroxenes in NWA 998.

Declaration of Competing Interest

The authors declare that they have no known competing financial interests or personal relationships that could have appeared to influence the work reported in this paper.

Acknowledgments

Thanks go to the Meteorite Working Group at Johnson Space Center for the 0.10 g sample of MIL 03346, 13, A.J. Irving for the 0.4 g sample of NWA 998, and C. Smith of the Natural History Museum in London for (0.25 g) Nakhla sample labelled BM. 1913, 25 (loaned to MC Domeneghetti and AM Fioretti). The authors gratefully acknowledge beamtime allocation and support from the Diamond Light Source under proposal sp9914-2 and all members of the I18 beamline team. Gloria Tognon is thanked for her work on quantifying the SXRF analyses and Jacopo Nava is thanked for his help on the SEM. We thank one anonymous reviewer and J. Filiberto for their useful and constructive reviews that improved this paper. A.M. acknowledges support by grant PRIN (20178LPCP); A. M.K. acknowledges support from Research Council of Norway through its Centres of Excellence funding scheme, project number 223272; S.C. acknowledges support from the Research Council of Norway (Young Research Talents project 301096); D.R.B. thanks NSERC for the Discovery grant that funded some of this research.

Appendix A. Supplementary material

1. Major element analyses of crystals by electron microprobe. 2. Locations of Synchrotron X-ray Fluorescence analyses. 3. Synchrotron X-ray Fluorescence maps of clinopyroxene crystals D-1, D-4 from MIL 03346, and 6-1 from Nakhla. 4. Ti/Al geothermometry. 5. Investigation of post-magmatic alteration. 6. Sulfide saturation of the clinopyroxene core parental melts. Supplementary material to this article that includes the data for this research not in Table 1 can be found online at https://doi.org/10.1016/j.gca.2023.08.007.

References

Albarède, F., 2009. Volatile accretion history of the terrestrial planets and dynamic implications. Nature 461, 1227–1233.
Alletti, M., Baker, D.R., Freda, C., 2007. Halogen diffusion in a basaltic melt. Geochim. Cosmochim. 71, 3570–3580.
Alvaro, M., Domeneghetti, M.C., Fioretti, A.M., Cámara, F., Marinangeli, L., 2015. A new calibration to determine the closure temperatures of Fe-Mg ordering in augite from nakhlites. Meteorit. Planet. Sci. 50, 499–507.
Baker, D.R., Balcone-Boissard, H., 2009. Halogen diffusion in magmatic systems: Our current state of knowledge. Chem. Geol. 263, 82–88.
Baker, D.R., Moretti, R., 2011. Modeling the solubility of sulfur in magmas: A 50-year old geochemical challenge. Rev. Mineral. Geochem. 73, 167–213.
Baker, D.R., Callegaro, S., De Min, A., Whitehouse, M.J., Marzoli, A., 2022. Fluorine partitioning between quadrilateral clinopyroxenes and melt. Am. Mineral. 107, 167–177.
Balta, J.B., Sanborn, M.E., Mayne, R.G., Wadhwa, M., McSween, H.Y., Crossley, S.D., 2017. Northwest Africa 5790: a previously unsampled portion of the upper part of the nakhlite pile. Meteorit. Planet. Sci. 52, 36–59.
Barnum, T.P., Coates, J.F., 2022. The biogeochemical cycling of chlorine. Geobiology 20, 634–639.
Beck, P., Barrat, J.A., Gillet, P., Wadhwa, M., Franchi, I.A., Greenwood, R.C., Bohn, M., Cotten, J., van de Moortèle, B., Reynard, B., 2006. Petrography and geochemistry of the chassignite Northwest Africa 2737 (NWA 2737). Geochim. Cosmochim. Acta 70, 2127–2139.
Bertka, C.M., Fei, Y., 1997. Mineralogy of the Martian interior up to core-mantle boundary pressures. J. Geophys. Res. 102, 5251–5264.
Bertka, C.M., Holloway, J.R., 1994. Anhydrous partial melting of an iron-rich mantle II: primary melt compositions at 15 kbar. Contrib. Mineral. Petrol. 115, 323–338.
Bonechi, B., Perinelli, C., Gaeta, M., 2020. Clinopyroxene growth rates at high pressure: constraints on magma recharge of the deep reservoir of the Campi Flegrei Volcanic District (south Italy). Bull. Volcan. 82, 5.

Boynton, W.V., Taylor, G.J., Evans, L.G., Reedy, R.C., Starr, R., Janes, D.M., Kerry, K.E., Drake, D.M., Kim, K.J., Williams, R.M.S., Crombie, M.K., Dohm, J.M., Baker, V., Metzger, A.E., Karunatillake, S., Keller, J.M., Newsom, H.E., Arnold, J.R., Brückner, J., Englert, P.A.J., Gasnault, O., Sprague, A.L., Mitrofanov, I., Squyres, S. W., Trombka, J.I., d'Uston, L., Wänke, H., Hamara, D.K., 2007. Concentration of H, Si, Cl, K, Fe and Th in the low- and mid-latitude regions of Mars. J. Geophys Res. Planets 112, E12S99.

Bridges, J.C., Grady, M.M., 1999. A halite-siderite-anhydrite-chlorapatite assemblage in Nakhla: Mineralogical evidence for evaporites on Mars. Meteorit. Planet. Sci. 34, 407–415.

Bridges, J.C., Grady, M.M., 2000. Evaporite mineral assemblages in nakhlite (martian) meteorites. Earth Planet. Sci. Lett. 176, 267–279.

Bridges, J.C., Schwenzer, S.P., 2012. The nakhlite hydrothermal brine on Mars. Earth Planet. Sci. Lett. 359–360, 117–123.

Callegaro, S., Geraki, K., Marzoli, A., De Min, A., Maneta, V., Baker, D.R., 2020. The quintet completed: the partitioning of sulfur between nominally volatile-free minerals and silicate melts. Am. Mineral. 105, 697–707.

Carraro, A., Fioretti, A., Domeneghetti, M.C., Rapsaet, C., Bureau, H., Cámara, F., Goodrich, C.A., 2010. Hydrogen contents in clinopyroxene from Martian meteorites (nakhlites) using Elastic Recoil Detection Analysis. 89° SIMP meeting "L'evoluzione del Sistema Terra dagli atomi ai vulcani" Ferrara 12–15 September (https://iris.unito.it/handle/2318/87341).

Certini, G., Karunatillake, S., Zhao, Y.-Y.-S., Meslin, P.-Y., Cousin, A., Hood, D.R., Scalenghe, R., 2020. Disambiguating the soils of Mars. Planet. Space Sci. 186, 104922.

Changela, H.G., Bridges, J.C., 2011. Alteration assemblages in the nakhlites: Variation with depth on Mars. Meteorit. Planet. Sci. 45, 1847–1867.

Clay, P.L., Joy, K.H., O'Driscoll, B., Busemann, H., Ruzié-Hamilton, L., Burgess, R., Fellowes, J., Joachim-Mrosko, B., Pernet-Fisher, J., Strekopytov, S., Ballentine, C., 2020. Heavy halogen geochemistry of martian shergottite meteorites and implications for the halogen composition of the depleted shergottite mantle source. Am. Mineral. 105, 289–306.

Cohen, B.E., Mark, D.F., Cassata, W.S., Lee, M.R., Tomkinson, T., Smith, C.L., 2017. Taking the pulse of Mars via dating a plume-fed volcano. Nature Commun. 8, 640.

Corrigan, C.M., Velbel, M.A., Vincenzi, E.P., 2015. Modal abundances of pyroxene, olivine, and mesostasis in nakhlites: Heterogeneity, variation, and implications for nakhlite emplacement. Meteorit. Planet. Sci. 50, 1497–1511.

Dahl, C., Friedrich, C.G. (Eds.), 2008. Microbial Sulfur Metabolism. Springer, Berlin, New York, p. 308.

Dalou, C., Koga, K.T., Shimizu, N., Boulon, J., Devidal, J.-L., 2012. Experimental determination of F and Cl partitioning between lherzolite and basaltic melt. Contrib. Mineral. Petrol. 163, 591–609.

Dalou, C., Koga, K.T., Le Voyer, M., Shimizu, N., 2014. Contrasting partition behavior of F and Cl during hydrous mantle melting: Implications for Cl/F in arc magmas. Progress Earth Planet. Sci. 1, 26.

Daly, L., Lee, M.R., Piazolo, S., Griffin, S., Bazargan, M., Campanale, F., Chung, P., Cohen, B.E., Pickersgill, A.E., Hallis, L.J., Trimby, P.W., Baumgartner, R., Forman, L. V., Benedix, G.K., 2019. Boom boom pow: Shock-facilitated aqueous alteration and evidence for two shock events in the Martian nakhlite meteorites. Sci. Adv. 5, eaaw5549.

Day, J.M.D., Taylor, L.A., Floss, C., McSween Jr., H.Y., 2006. Petrology and chemistry of MIL 03346 and its significance in understanding the petrogenesis of nakhlites on Mars. Meteorit. Planet. Sci. 41, 581–606.

Day, J.M.D., Tait, K.T., Udry, A., Moynier, F., Liu, Y., Neal, C.R., 2018. Martian magmatism from plume metasomatized mantle. Nature Commun. 9, 4799.

DePaolo, D.J., 1981. Trace element and isotopic effect of combined wallrock assimilation and fractional crystallization. Earth. Planet Sci. Lett. 53, 189–202.

Ding, S., Dasgupta, R., 2017. The fate of sulfide during decompression melting of peridotite – Implications for sulfur inventory of the MORB-source depleted upper mantle. Earth Planet. Sci. Lett. 459, 183–195.

Ding, S., Dasgupta, R., Lee, C.-T.-A., Wadhwa, M., 2015. New bulk sulfur measurements of Martian meteorites and modeling the fate of sulfur during melting and crystallization – Implications for sulfur transfer from martian mantle to crust-atmosphere system. Earth Planet. Sci. Lett. 409, 157–167.

Domeneghetti, M.C., Fioretti, A.M., Cámara, F., McCammon, C., Alvaro, M., 2013. Thermal history of nakhlites: A comparison between MIL 03346 and its terrestrial analogue Theo's Flow. Geochim. Cosmochim. Acta 121, 571–581.

Dreibus, G., Wänke, H., 1987. Volatiles on Earth and Mars: A comparison. Icarus 71, 225–240.

Farquhar, J., Savarino, J., Jackson, T.L., Thiemens, M.H., 2000. Evidence of atmospheric sulphur in the martian regolith from sulphur isotopes in meteorites. Nature 404, 50–52.

Filiberto, J., Dasgupta, R., 2011. Fe^{2+} - Mg partitioning between olivine and basaltic melts: Applications to genesis of olivine-phyric shergottites and conditions of melting in the Martian interior. Earth. Planet Sci. Lett. 304, 527–537.

Filiberto, J., Gross, J., McCubbin, F.M., 2016. Constraints in the water, chlorine, and fluorine content of the Martian mantle. Meteorit. Planet. Sci. 51, 2023–2035.

Filiberto, J., McCubbin, F.M., Taylor, G.J., 2019. Volatiles in martian magmas and the interior: Inputs of volatiles into the crust and atmosphere. In: Filiberto, J., Schwenzer, S.P. (Eds.), Volatiles in the Martian Crust. Elsevier, Amsterdam, pp. 13–33.

Filiberto, J., Treiman, A.H., 2009a. The effect of chlorine on the liquidus of basalt: First results and implications for basalt genesis on Mars and Earth. Chem. Geol. 263, 60–68.

Filiberto, J., Treiman, A.H., 2009b. Martian magmas contained abundant chlorine, but little water. Geology 37, 1087–1090.

Filiberto, J., Treiman, A.H., Giesting, P.A., Goodrich, C.A., Gross, J., 2014. High-temperature chlorine-rich fluid in the martian crust: A precursor to habitability. Earth Planet. Sci. Lett. 401, 110–115.

Franz, H.B., Kim, S.-T., Farquhar, J., Day, J.M.D., Economos, R.C., McKeegan, K.D., Schmitt, A.K., Irving, A.J., Hoek, J., Dottin III, J., 2014. Isotopic links between atmospheric chemistry and the deep sulphur cycle on Mars. Nature 508, 364–368.

Franz, H.B., Wu, N., Farquhar, J., Irving, A.J., 2019. A new type of isotopic anomaly in shergottite sulfides. Meteor. Planet. Sci. 54, 3036–3051.

Freda, C., Baker, D.R., Scarlato, P., 2005. Sulfur diffusion in basaltic melts. Geochim. Cosmochim. Acta 69, 5061–5069.

Frezzotti, M.L., Ferrando, S., 2018. The role of halogens in the lithospheric mantle. In: Harlov, D., Aranovich, L. (Eds.), The Role of Halogens in Terrestrial and ExtraTerrestrial Geochemical Processes. Springer-Verlag, Heidelberg, pp. 805–845.

Fritz, J., Artemieva, N., Greshake, A., 2005a. Ejection of Martian meteorites. Meteor. Planet. Sci. 40, 1393–1411 (see Appendix A. Supplementary Materials).

Fritz, J., Greshake, A., Stöffler, D., 2005b. Micro-Raman spectroscopy of plagioclase and maskelynite in martian meteorites: evidence of progressive shock metamorphism. Antarct. Meteorite Res. 18, 98–116 (see Appendix A. Supplementary Materials).

Gaillard, F., Michalski, J., Berger, G., McLennan, S.M., Scaillet, B., 2013. Geochemical reservoirs and timing of sulfur cycling on Mars. Space Sci. Rev. 174, 251–300.

Giesting, P.A., Filiberto, J., 2016. The formation environment of potassic-chloro-hastingsite in the nakhlites MIL 03346 and pairs and NWA 5790: Insights from terrestrial chloro-amphibole. Meteorit. Planet. Sci. 11, 2127–2153.

Gillet, Ph., Barrat, J.A., Deloule, E., Wadhwa, M., Jambon, A., Sautter, V., Devouard, B., Neuville, D., Benzerara, K., Lesourd, M., 2002. Aqueous alteration in the Northwest Africa 817 (NWA 817) Martian meteorite. Earth. Planet. Sci. Lett. 203, 431-444.

Giuliani, L., Iezzi, G., Vetere, F., Behrens, H., Mollo, S., Cauti, F., Ventura, G., Scarlato, P., 2020. Evolution of textures, crystal size distributions and growth rates of plagioclase, clinopyroxene and spinel crystallized at variable cooling rates from a mid-ocean ridge basaltic melt. Earth Sci. Rev. 204, 103165-1.

Goldstein, J., Newbury, D., Joy, D., Lyman, C., Echlin, P., Lifshin, E., Sawyer, L., Michael, J., 2003. Scanning Electron Microscopy and X-ray Microanalysis, 3rd ed. Springer, New York, pp. 1–690.

Goodrich, C.A., Treiman, A.H., Filiberto, J., Gross, J., Jercinovic, M., 2013. K_2O-rich trapped melt in olivine in the Nakhla meteorite: Implications for petrogenesis of nakhlites and evolution of the Martian mantle. Meteorit. Planet. Sci. 48, 2371–2405.

Hallis, L.J., Taylor, G.J., 2011. Comparisons of the four Miller Range nakhlites, MIL 03346, 090030, 090032 and 090136: Textural and compositional observations of primary and secondary mineral assemblages. Meteorit. Planet. Sci. 46, 1787–2011.

Hammer, J.E., 2009. Application of a textural geospeedometer to the late-stage magmatic history of MIL 03346. Meteorit. Planet. Sci. 44, 141–154.

Harrison, T.M., Watson, E.B., 1984. The behavior of apatite during crustal anatexis: equilibrium and kinetic considerations. Geochim. Cosmochim. Acta 48, 1467–1477.

Harvey, R.P., McSween Jr., H.Y., 1992. The parent magma of the nakhlite meteorites: Clues from melt inclusions. Earth Planet. Sci. Let. 111, 467–482.

Imae, N., Ikeda, Y., 2007. Petrology of the Miller Range 03346 nakhlite in comparison with the Yamato-00593 nakhlite. Meteorit. Planet. Sci. 42, 171–184.

Imae, N., Ikeda, Y., 2008. Crystallization experiments on intercumulus melts for nakhlites under QFM ± 2 at 1 bar. Meteorit. Planet. Sci. 43, 1299–1319.

Jambon, A., Sautter, V., Barrat, J.-A., Gattacceca, J., Rochette, P., Boudouma, O., Badia, D., Devouard, B., 2016. Northwest Africa 5790: Revisiting nakhlite petrogenesis. Geochim. Cosmochim. Acta 190, 191–212.

Jørgensen, B.B., 2021. Sulfur biogeochemical cycle of marine sediments. Geochem. Perspect. 10, 145–307.

Konecke, B.A., Fiege, A., Simon, A.D., Holtz, F., 2017. Cryptic metasomatism during late-stage lunar magmatism implicated by sulfur in apatite. Geology 46, 739–742.

Korochantseva, E.V., Schwenzer, S.P., Buikin, A.I., Hopp, J., Ott, U., Trieloff, M., 2011. ^{40}Ar-^{39}Ar and cosmic-ray exposure ages of nakhlites—Nakhla, Lafayette, Governador Valadares—and Chassigny. Meteorit. Planet. Sci. 46, 1397–1417.

Lentz, R.C.F., Taylor, G.J., Treiman, A.H., 1999. Formation of a Martian pyroxenite: A comparative study of the nakhlite meteorites and Theo's flow. Meteorit. Planet. Sci. 34, 919–932.

Lentz, R.C.F., McCoy, T.J., Collins, L.E., Corrigan, C.M., Benedix, G.K., Taylor, G.J., Harvey, R.P., 2011. Theo's Flow, Ontario, Canada: A terrestrial analog for the Martian nakhlite meteorites. In: Garry, W.B., Bleacher, J.E. (Eds.), Analogs for Planetary Exploration, 483. Geological Society of America Special Paper, pp. 263–277.

Lessel, J., Putirka, K., 2015. New thermobarometers for martian igneous rocks, and some implications for secular cooling on Mars. Am. Mineral. 100, 2163–2171.

Lodders, K., Fegley Jr., B., 1997. An oxygen isotope model for the composition of Mars. Icarus 126, 373–394.

Longhi, J., Pan, V., 1989. The parent magmas of the SNC meteorites. In: Proceedings, Lunar Planet. Sci., XIX. Lunar Planet. Inst, Houston, pp. 451–464.

Mari, N., Rihes, A.J.V., Hallis, L.J., Marrocchi, Y., Villeneuve, J., Gleissner, P., Becker, H., Lee, M.R., 2019. Syneruptive incorporation of martian surface sulphur in the nakhlite lava flows revealed by S and Os isotopes and highly siderophile elements: implication for mantle sources in Mars. Geochim. Cosmochim. Acta 266, 416–434.

Martell, J., Alwmark, C., Daly, L., Hall, S., Alwmark, S., Woracek, R., Hektor, J., Helfen, L., Tengattini, A., Lee, M., 2022. The scale of martian hydrothermal system explored using combined neutron and X-ray tomography. Sci. Adv. 8, eabn3044.

Matsukage, K.N., Nagayo, Y., Whitaker, M.L., Takahashi, E., Kawasaki, T., 2013. Melting of the Martian mantle from 1.0 to 4.5 GPa. J. Mineral Petrol. Sci. 108, 201–214.

McCubbin, F.M., Tosca, N.J., Smirnov, A., Nekvasil, H., Steele, A., Fries, M., Lindsley, D. H., 2009. Hydrothermal jarosite and hematite in a pyroxene-hosted melt inclusion in martian meteorite Miller Range (MIL) 03346: Implications for magmatic-hydrothermal fluids on Mars. Geochim. Cosmochim. Acta 73, 4907–4917.

McCubbin, F.M., Elardo, S.M., Shearer Jr., C.K., Smirnov, A., Hauri, E.H., Draper, D.S., 2013. A petrogenetic model for the comagmatic origin of chassignites and nakhlites: Inferences from chlorine-rich minerals, petrology, and geochemistry. Meteorit. Planet. Sci. 48, 819–853.
McCubbin, F.M., Boyce, J.W., Srinivasan, P., Santos, A.R., Elardo, S.M., Filiberto, J., Steele, A., Shearer, C.K., 2016. Heterogeneous distribution of H_2O in the Martian interior: Implications for the abundance of H_2O in depleted and enriched mantle sources. Meteorit. Planet. Sci. 51, 2036–2060.
Mikouchi, T., Koizumi, E., Monkawa, A., Ueda, Y., Miyamoto, M., 2003. Mineralogy and petrology of Yamato 000593: Comparison with other Martian nakhlite meteorites. Antarct. Meteor. Res. 16, 34–57.
Mikouchi, T., Miyamoto, M., 2002. Comparative cooling rates of nakhlites as inferred from iron-magnesium and calcium zoning of olivines. Lunar Planet. Sci. XXXIII. Abstr. 1343.
Morrison, S.M., Downs, R.T., Blake, D.F., Vaniman, D.T., Ming, D.W., Hazen, R.M., Treiman, A.H., Achilles, C.N., Yen, A.S., Morris, R.V., Rampe, E.B., Bristow, T.F., Chipera, S.J., Sarrazin, P.C., Gellert, R., Fendrich, K.V., Morookian, J.M., Farmer, J. D.D., Maris, D.J., Craig, P.I., 2018. Crystal chemistry of martian minerals from Bradbury Landing through Naukluft Plateau, Gale crater. Mars. Am. Mineral. 103, 857–871.
Murri, M., Scandolo, L., Fioretti, A.M., Nestola, F., Domeneghetti, M.C., Alvaro, M., 2016. The role of Fe content on the Fe-Mg exchange reaction in augite. Am. Mineral. 101, 2747–2750.
Murri, M., Domeneghetti, M.C., Fioretti, A.M., Nestola, F., Vetere, F., Perugini, D., Pisello, A., Faccenda, M., Alvaro, M., 2019. Cooling history and emplacement of a pyroxenitic lava as proxy for understanding Martian lava flows. Sci. Rep. 9, 17051.
Neave, D.A., Putirka, K.D., 2017. A new clinopyroxene-liquid barometer, and implications for magma storage pressures under Icelandic rift zones. Am. Mineral. 102, 777–794.
Nekvasil, H., Filiberto, J., McCubbin, F.M., Lindsley, D.H., 2007. Alkalic parental magmas for chassignites? Meteorit. Planet. Sci. 42, 979–992.
Nielsen, S.G., Shimizu, N., Lee, C.-T.-A., Behn, M.D., 2014. Chalcophile behavior of thallium during MORB melting and implications for the sulfur content of the mantle. Geochem. Geophys. Geosyst. 15, 4905–4919.
Noguchi, T., Nakamura, T., Misawa, K., Imae, N., Aoki, T., Toh, S., 2009. Laihunite and jarosite in the Yamato 00 nakhlites: Alteration products on Mars? J. Geophys. Res. 114, E10004.
Paquet, M., Day, J.M.D., Udry, A., Hattingh, R., Kumler, B., Rahib, R.R., Tait, K.T., Neal, C.R., 2021. Highly siderophile elements in the shergottite sulfides and sulfur content of the martian mantle. Geochim. Cosmochim. Acta 292, 279–298.
Paquette, J., Reeder, R.J., 1990. New type of compositional zoning in calcite: Insights into crystal-growth mechanisms. Geology 18, 1244–1247.
Peslier, A.H., Hervig, R., Yang, S., Humayun, M., Barnes, J.J., Irving, A.J., Brandon, A.D., 2019. Determination of the water content and D/H ratio of the martian mantle by unraveling degassing and crystallization effects in nakhlites. Geochim. Cosmochim. Acta 266, 382–415.
Pontesilli, A., Masotta, M., Nazzari, M., Mollo, S., Armienti, P., Scarlato, P., Brenna, M., 2019. Crystallization kinetics of clinopyroxene and titanomagnetite growing from a trachybasaltic melt: New insights from isothermal time-series experiments. Chem. Geol. 510, 113–129.
Rampe, E.B., Blake, D.F., Bristow, T.F., Ming, D.W., Vaniman, D.T., Morris, R.V., Achilles, G.N., Chipera, S.J., Morrison, S.M., Tu, V.M., Yen, A.S., Castle, N., Downs, G.W., Downs, R.T., Grotzinger, J.P., Hazen, R.M., Treiman, A.H., Peretyazhko, T.S., Des Marais, D.J., Walroth, R.C., Craig, P.I., Crisp, J.A., Lafuente, B., Morookian, J.M., Sarrazin, P.C., Thorpe, M.T., Bridges, J.C., Edgar, L. A., Fedo, C.M., Freissinet, C., Gellert, R., Mahaffy, P.R., Newsom, H.E., Johnson, J.R., Kah, L.C., Siebach, K.L., Schieber, J., Sun, V.Z., Vasavada, A.R., Wellington, D., Wiens, R.C., 2020. Mineralogy and geochemistry of sedimentary rocks and eolian sediments in Gale crater, Mars: A review after six Earth years of exploration with Curiosity. Geochemistry 80, 125605.
Richter, F., Chaussidon, M., Mendybaev, R., Kite, E., 2016. Reassessing the cooling rate and geologic setting of Martian meteorites MIL 03346 and NWA 817. Geochim. Cosmochim. Acta 182, 1–23.
Righter, K., Pando, K., Danielson, L.R., 2009. Experimental evidence for sulfur-rich martian magmas: Implications for volcanism and surficial sulfur sources. Earth Planet. Sci. Lett. 288, 235–243.
Rousseau, R.M., 2001. Detection limit and estimate of uncertainty of analytical XRF results. Rigaku J. 18, 33–47.
Salters, V.J.M., Stracke, A., 2004. Composition of the depleted mantle. Geochem. Geophys. Geosyst. 5, Q05B07.
Sanloup, C., Jambon, A., Gillet, P., 1999. A simple chondritic model of Mars. Phys. Earth Planet. Int. 112, 43–54.
Sautter, V., Barrat, J.A., Jambon, A., Lorand, J.P., Gillet, P., Javoy, M., Joron, J.L., Lesourd, M., 2002. A new Martian meteorite from Morocco: The nakhlite North West Africa 817. Earth Planet. Sci. Lett. 195, 223–238.
Sautter, V., Jambon, A., Boudouma, O., 2006. Cl-amphibole in the nakhlite MIL 03346: Evidence for sediment contamination in a Martian meteorite. Earth. Planet. Sci. Lett. 252, 45–55.
Sautter, V., Toplis, M.J., Lorand, J.-P., Macri, M., 2012. Melt inclusions in augite from the nakhlite meteorites: A reassessment of nakhlite parental melt and implications for petrogenesis. Meteorit. Planet. Sci. 47, 330–344.
Semprich, J., Filiberto, J., 2020. High-pressure metamorphic mineralogy of the Martian crust with implications for density and seismic profiles. Meteorit. Planet. Sci. 56, 1600–1614.
Shaw, D.M., 1970. Trace element fractionation during anatexis. Geochim. Cosmochim. Acta 84, 237–243.
Shearer, C.K., Messenger, S., Sharp, Z.D., Burger, P.V., Nguyen, A.N., McCubbin, F.M., 2018. Distinct chlorine isotopic reservoirs on Mars. Implications for character, extent and relative timing of crustal interactions with mantle-derived magmas, evolution of the martian atmosphere, and the building blocks of an early Mars. Geochim. Cosmochim. Acta 234, 24–36.
Skulski, T., Minarik, W., Watson, E.B., 1994. High-pressure experimental trace-element partitioning between clinopyroxene and basaltic melts. Chem. Geol. 117, 127–147.
Smith, V.G., Tiller, W.A., Rutter, J.W., 1955. A mathematical analysis of solute distribution during solidification. Can. J. Phys. 33, 723–745.
Solé, V.A., Papillon, E., Cotte, M., Walter, P., Susini, J., 2007. A multiplatform code for the analysis of energy-dispersive X-ray fluorescence spectra. Spectrochim. Acta B 62, 63–68.
Steenstra, E.S., van Westrenen, W., 2018. A synthesis of geochemical constraints on the inventory of light elements in the core of Mars. Icarus 315, 69–78.
Stockstill, K.R., McSween Jr., H.Y., Bodnar, R.J., 2005. Melt inclusions in augite of the Nakhla martian meteorite: Evidence for basaltic parental melt. Meteorit. Planet. Sci. 40, 377–398.
Stopar, J.D., Lawrence, S.J., Lentz, R.C.F., Taylor, G.J., Velbel, M.A., Norman, M.D., Vincenzi, E.P., Hallis, J.J., 2013. Element abundances, patterns, and mobility in Nakhlite Miller Range 03346 and implications for aqueous alteration. Geochim. Cosmochim. Acta 112, 208–225.
Sun, Z., Xiong, X., Wang, J., Liu, X., Li, L., Ruan, M., Zhang, L., Takahashi, E., 2020. Sulfur abundance and heterogeneity in the MORB mantle estimated by copper partitioning and sulfur solubility modelling. Earth Planet. Sci. Lett. 538, 116169.
Taylor, G.J., 2013. The bulk composition of Mars. Chemie der Erde 74, 401–420.
Treiman, A.H., 2005. The nakhlite meteorites: Augite-rich igneous rocks from Mars. Chemie der Erde 65, 203–270.
Treiman, A.H., Irving, A.J., 2008. Petrology of martian meteorite Northwest Africa 998. Meteor. Planet. Sci. 43, 829–854.
Udry, A., Day, J.M.D., 2018. 1.34 billion-year-old magmatism on Mars evaluated from the co-genetic nakhlite and chassignite meteorites. Geochim. Cosmochim. Acta 238, 292–315.
Udry, A., McSween, H.Y., Lecumberri-Sanchez, P., Bodnar, R.J., 2012. Paired nakhlites MIL 90030, 090032, 090136, and 03346: Insights into the Miller Range parent meteorite. Meteor. Planet. Sci. 47, 1575–1589.
Udry, A., Howarth, G.H., Herd, C.D.K., Day, J.M.D., Lapen, T.J., Filiberto, J., 2020. What Martian meteorites reveal about the interior and surface of Mars. J. Geophys. Res. Planets 125, e2020JE006523.
Usui, T., Alexander, C.O.M'D, Wang, J., Simon, J.I., Jones, J.H., 2012. Origin of water and mantle-crust interactions on Mars inferred from hydrogen isotopes and volatile element abundances of olivine-hosted melt inclusions of primitive shergottites. Earth Planet. Sci. Lett. 357–358, 119–129.
Varela, M.E., Kurat, G., Clocchiatti, R., 2001. Glass-bearing inclusions in Nakhla (SNC meteorite) augite: Heterogeneously trapped phases. Contrib. Mineral. Petrol. 71, 155–172.
Wang, Z., Becker, H., 2017. Chalcophile elements in Martian meteorites indicate low sulfur content in the Martian interior and a volatile element-depleted late veneer. Earth Planet. Sci. Lett. 463, 56–68.
Wänke, H., Dreibus, G., 1988. Chemical composition and accretion history of terrestrial planets. Phil. Trans. R. Soc. Lond. A. 325, 545–557.
Watson, E.B., 1979. Apatite saturation in basic to intermediate magmas. Geophys. Res. Lett. 6, 937–940.
Watson, E.B., 1996. Surface enrichment and trace-element uptake during crystal growth. Geochim. Cosmochim. Acta 60, 5013–5020.
Webster, J.D., Aiuppa, A., Baker, D.R., 2018. Halogens in Mafic and Intermediate-Silica Content Magmas. In: Harlov, D., Aranovich, L. (Eds.), The Role of Halogens in Terrestrial and ExtraTerrestrial Geochemical Processes. Springer-Verlag, Heidelberg, pp. 307–430.
White, W.M., 2013. Geochemistry. Wiley-Blackwell, Chichester, p. 660.
Wieczorek, M.A., Broquet, A., McLennan, S.M., Rivoldini, A., Golombek, M., Antonangeli, D., Beghein, C., Giardini, D., Gudkova, T., Gyalay, S., Johnson, C.L., Joshi, R., Kim, D., King, S.D., Knapmeyer-Endrun, B., Lognonné, P., Michaut, C., Mittelholz, A., Nimmo, F., Ojha, L., Panning, M.P., Plesa, A.-C., Siegler, M.A., Smrekar, S.E., Spohn, T., Banerdt, W.B., 2022. Insight constraints on the global character of the martian crust. J. Geophys Res. Planets 127, e2022JE007298.
Yoshizaki, T., McDonough, W.F., 2020. The composition of Mars. Geochim. Cosmochim. Acta 273, 137–162.
Zajacz, Z., Candela, P.A., Piccoli, P.M., Sanchez-Valle, C., 2012. The partitioning of sulfur and chlorine between andesite melts and magmatic volatiles and the exchange coefficients of major cations. Geochim. Cosmochim. Acta 89, 81–101.
Zhang, R., Zhang, X., Guy, B., Hu, S., De Ligny, D., Moutte, J., 2013. Experimental study of dissolution rates of hedenbergitic clinopyroxene at high temperatures: Dissolution in water from 25 °C to 374 °C. Eur. J. Mineral. 25, 353–372.